Article

Exploration of the Crystal Structure and Thermal and Spectroscopic Properties of Monoclinic Praseodymium Sulfate $Pr_2(SO_4)_3$

Yuriy G. Denisenko [1,2,3], Victor V. Atuchin [4,5,6,7,8,*], Maxim S. Molokeev [9,10,11], Alexander E. Sedykh [3], Nikolay A. Khritokhin [1], Aleksandr S. Aleksandrovsky [12,13], Aleksandr S. Oreshonkov [14,15], Nikolai P. Shestakov [14], Sergey V. Adichtchev [16], Alexey M. Pugachev [16], Elena I. Sal'nikova [1,17], Oleg V. Andreev [1], Illaria A. Razumkova [1] and Klaus Müller-Buschbaum [3,18]

1   Department of Inorganic and Physical Chemistry, Tyumen State University, 625003 Tyumen, Russia;
    yu.g.denisenko@gmail.com (Y.G.D.); kna@utmn.ru (N.A.K.); elenasalnikova213@gmail.com (E.I.S.);
    o.v.andreev@utmn.ru (O.V.A.); razumkova@list.ru (I.A.R.)
2   Department of General and Special Chemistry, Industrial University of Tyumen, 625000 Tyumen, Russia
3   Institute of Inorganic and Analytical Chemistry, Justus-Liebig-University Giessen, 35392 Giessen, Germany;
    alexander.sedykh@anorg.chemie.uni-giessen.de (A.E.S.);
    klaus.mueller-buschbaum@anorg.chemie.uni-giessen.de (K.M.-B.)
4   Laboratory of Optical Materials and Structures, Institute of Semiconductor Physics, SB RAS,
    630090 Novosibirsk, Russia
5   Research and Development Department, Kemerovo State University, 650000 Kemerovo, Russia
6   Department of Applied Physics, Novosibirsk State University, 630090 Novosibirsk, Russia
7   Department of Industrial Machinery Design, Novosibirsk State Technical University,
    630073 Novosibirsk, Russia
8   R&D Center "Advanced Electronic Technologies", Tomsk State University, Tomsk 634034, Russia
9   Laboratory of Crystal Physics, Kirensky Institute of Physics, Federal Research Center KSC SB RAS,
    660036 Krasnoyarsk, Russia; msmolokeev@mail.ru
10 School of Engineering Physics and Radio Electronics, Siberian Federal University, 660041 Krasnoyarsk, Russia
11 Department of Physics, Far Eastern State Transport University, 680021 Khabarovsk, Russia
12 Laboratory of Coherent Optics, Kirensky Institute of Physics Federal Research Center KSC SB RAS,
    660036 Krasnoyarsk, Russia; aleksandrovsky@kirensky.ru
13 Institute of Nanotechnology, Spectroscopy and Quantum Chemistry, Siberian Federal University,
    660041 Krasnoyarsk, Russia
14 Laboratory of Molecular Spectroscopy, Kirensky Institute of Physics Federal Research Center KSC SB RAS,
    660036 Krasnoyarsk, Russia; oreshonkov@iph.krasn.ru (A.S.O.); nico@iph.krasn.ru (N.P.S.)
15 School of Engineering and Construction, Siberian Federal University, 660041 Krasnoyarsk, Russia
16 Institute of Automation and Electrometry, Russian Academy of Sciences, 630090 Novosibirsk, Russia;
    adish2@ngs.ru (S.V.A.); apg@iae.nsk.su (A.M.P.)
17 Research Department, Northern Trans-Ural Agricultural University, 625003 Tyumen, Russia
18 Center for Materials Research (LaMa), Justus-Liebig-University Giessen, 35392 Giessen, Germany
*   Correspondence: atuchin@isp.nsc.ru

Abstract: Praseodymium sulfate was obtained by the precipitation method and the crystal structure was determined by Rietveld analysis. $Pr_2(SO_4)_3$ is crystallized in the monoclinic structure, space group $C2/c$, with cell parameters a = 21.6052 (4), b = 6.7237 (1) and c = 6.9777 (1) Å, β = 107.9148 (7)°, Z = 4, V = 964.48 (3) Å^3 (T = 150 °C). The thermal expansion of $Pr_2(SO_4)_3$ is strongly anisotropic. As was obtained by XRD measurements, all cell parameters are increased on heating. However, due to a strong increase of the monoclinic angle β, there is a direction of negative thermal expansion. In the argon atmosphere, $Pr_2(SO_4)_3$ is stable in the temperature range of T = 30–870 °C. The kinetics of the thermal decomposition process of praseodymium sulfate octahydrate $Pr_2(SO_4)_3 \cdot 8H_2O$ was studied as well. The vibrational properties of $Pr_2(SO_4)_3$ were examined by Raman and Fourier-transform infrared absorption spectroscopy methods. The band gap structure of $Pr_2(SO_4)_3$ was evaluated by ab initio calculations, and it was found that the valence band top is dominated by the p electrons of oxygen ions, while the conduction band bottom is formed by the d electrons of Pr^{3+} ions. The exact position of ZPL is determined via PL and PLE spectra at 77 K to be at 481 nm, and that enabled a

correct assignment of luminescent bands. The maximum luminescent band in $Pr_2(SO_4)_3$ belongs to the $^3P_0 \rightarrow {}^3F_2$ transition at 640 nm.

1. Introduction

Rare earth (Ln) containing crystals exhibit exceptional material properties with wide-ranging technological significance [1–4]. The materials are widely used in solid-state laser devices, nonlinear optics and electronic and photonic systems because of their unique electron level configuration and specific chemical properties [5–17]. As to the crystal chemistry of Ln-containing compounds, it is based on the existence of the element range from La to Lu with a continuous variation of effective radius of Ln^{3+} ions that, in many cases, governs the boundaries of particular structure types [18]. Accordingly, structural, thermal and optical properties can be tuned by the substitution of Ln^{3+} ions. A lot of such inorganic crystal families can be found in the literature for different anion types, and the crystals with $(SO_4)^{2-}$ units are among less studied ones. As may be reasonably assumed, this state of things was formed due to the known effect of high hygroscopicity of sulfate compounds, and that greatly complicates their synthesis and use in precise electronic and optical technologies. Nevertheless, sulfate materials are traditionally applied in building industry, the extraction of Ln elements from natural and waste sources and catalysis [19–27].

In recent years, sulfate crystals have been actively studied in the general flow of searching new optical materials transparent in the UV spectral range, and many novel materials with interesting linear and nonlinear optical properties were discovered [28–42]. Some specific features were found in the coordination of $(SO_4)^{2-}$ anions in the crystal lattice [41]. However, there are no sufficient data on the structure of many known sulfate compounds for a proper classification and property analysis. In particular, despite the redundancy of the data on the crystal structures and properties of rare-earth sulfate hydrates $Ln_2(SO_4)_3 \cdot xH_2O$, most of the corresponding anhydrous phases with general composition $Ln_2(SO_4)_3$ are not even structurally characterized. To date, only the crystal structures of two sulfates of light rare-earth elements, namely $Nd_2(SO_4)_3$ [43] and $Eu_2(SO_4)_3$ [44], have been described in detail. It was established that both phases crystallize in the monoclinic system, space group $C2/c$. As to sulfates of heavy rare-earth elements, crystal structures are available for $Ln_2(SO_4)_3$, Ln = Y [45], Er [46] and Yb [47] compounds. These materials are predominantly crystallized in the orthorhombic system, space group *Pbcn*. Moreover, the noncentrosymmetric trigonal polymorphic modification was reported for $Yb_2(SO_4)_3$ (space group $R3c$) [44], and a trigonal structure (space group R-$3c$) was observed in closely related sulfate $Sc_2(SO_4)_3$ [48]. Thus, the crystal chemistry of $Ln_2(SO_4)_3$ compounds is not simple, and the appearance of different structure types is possible depending on the Ln element and formation conditions.

The present study is aimed at the preparation of $Pr_2(SO_4)_3$ and the evaluation of its structural, thermal and spectroscopic characteristics. This contribution allows evaluating the composition boundaries of the existence of monoclinic structure in anhydrous sulfates $Ln_2(SO_4)_3$. As is known, praseodymium, due to its peculiar electronic structure, may be in different valence states and exhibits various coordination environments in the crystal lattice [49–55]. Praseodymium ions are able to accept an oxygen deficiency in oxide systems, thereby causing the photocatalytic activity of Pr-containing compounds [55–61]. The systems with the Pr^{3+} ions could exhibit interesting spectroscopic properties as promising optical and luminescent materials [62–68]. Accordingly, the characterization of Pr-containing sulfates is of particular interest. In this work, anhydrous sulfate $Pr_2(SO_4)_3$ was synthesized by the chemical precipitation method, and its structural and thermophysical parameters were determined on the base of X-ray diffraction measurements. The thermal stability of the sulfate was evaluated by simultaneous DTA/TG measurements. The

vibrational properties of $Pr_2(SO_4)_3$ were obtained by IR and Raman spectral analyses. Then, photoluminescence effects were comparatively evaluated at 77 and 300 K.

2. Methods and Materials

Praseodymium (III) sulfate $Pr_2(SO_4)_3$ was synthesized by the precipitation from a solution of $Pr(NO_3)_3$. Pr_6O_{11} (99.99%, ultrapure, TDM-96 Ltd., Ekaterinburg, Russia), concentrated nitric acid solution ($C(HNO_3)$ = 14.6 mol/L, ultrapure, Vekton Ltd., St. Petersburg, Russia) and concentrated sulfuric acid solution ($C(H_2SO_4)$ = 17.9 mol/L, ultrapure, Vekton Ltd., St. Petersburg, Russia) were used as the starting reagents. Weighing the dry reagents was carried out on an analytical balance of the accuracy of 0.1 mg. Praseodymium oxide, prior to weighing, was calcined in a muffle furnace at the temperature of 1000 °C for 12 h to remove the gases adsorbed from the air and the products of their interaction with the Pr_6O_{11} surface. The acid solutions were measured by means of glass measuring cylinders with an accuracy of 0.1 mL.

First, the 2.9866 g Pr_6O_{11} charge was placed in a 100 mL glass round-bottomed flask. Then, 3.6 mL of the concentrated nitric acid solution was added in small portions. The reaction mixture was heated with a continuous stirring until the oxide was completely dissolved. As a result, the praseodymium (III) nitrate solution was obtained by redox reaction:

$$Pr_6O_{11} + 18HNO_3 \rightarrow 6Pr(NO_3)_3 + 9H_2O + O_2 \tag{1}$$
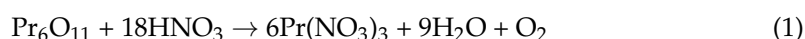
After cooling the solution to room temperature, 1.6 mL (an excess of 10%) of the concentrated sulfuric acid solution was added to the flask in small portions, not allowing a strong reheating of the reaction mixture. The reaction results in the praseodymium sulfate precipitation:

$$2Pr(NO_3)_3 + 3H_2SO_4 \rightarrow Pr_2(SO_4)_3\downarrow + 6HNO_3 \tag{2}$$
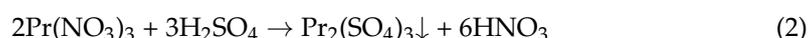
After the precipitation, the mixture was distilled to a dry residue. The praseodymium sulfate powder was additionally calcined in a tubular furnace at 500 °C to remove the adsorbed acid and then annealed in a muffle furnace at the same temperature for 7 days to form the final powder product. According to the synthesis steps described above, 4.9672 g of praseodymium sulfate powder were obtained. The yield of the target product is 99% of the theoretical level. According to the gravimetric analysis, the content of sulfate ions in the resulting compound is 50.58%. At the theoretical value of 50.56% for $Pr_2(SO_4)_3$, the possible determination error is 0.5%, which corresponds to the relative error for this analytical method. As seen in the photo shown in Figure S1a, the synthesized powder of praseodymium sulfate has a light green tint, which is a common characteristic of Pr^{3+}-containing oxides.

Praseodymium (III) sulfate octahydrate $Pr_2(SO_4)_3 \cdot 8H_2O$ was obtained by the crystallization from an aqueous saturated solution at room temperature in a vacuum desiccator under reduced pressure. A saturated solution was prepared by dissolving anhydrous praseodymium (III) sulfate $Pr_2(SO_4)_3$ (chemically pure) weighing 2.50 g in 100 mL of deionized water at the temperature of 20 °C. The precipitate formed by crystallization was separated from the mother liquor, squeezed between filter paper sheets and kept at room temperature on watching glass in a desiccator with calcined silica gel to reach a constant weight. Thus, light green shiny crystals of praseodymium (III) sulfate octahydrate $Pr_2(SO_4)_3 \cdot 8H_2O$ were obtained. A photo of this powder product is shown in Figure S1b. As is evident, the colors of both $Pr_2(SO_4)_3$ and $Pr_2(SO_4)_3 \cdot 8H_2O$ are in the green color spectrum, but the tints are different, which could be attributed to the difference in the crystal structure and the presence of H_2O units.

The structural properties of the powder samples were obtained by the X-ray diffraction analysis with the use of a Bruker D8 ADVANCE powder diffractometer (Cu-Kα radiation) and linear VANTEC detector. The step size of 2θ was 0.016°, and the integration time was 3 s per step. First, to evaluate the chemical stability of the $Pr_2(SO_4)_3$ sample, several XRD

patterns were collected each 30 min in contact with the laboratory air at room temperature, normal pressure and humidity (Figure S2). As the X-ray patterns noticeably changed with the exposure time increase, it was concluded that the sample absorbs water from the air, leading to the formation of intermediate hydrated phases. Therefore, to exclude the hydration effects, the powder data for Rietveld analysis were collected at 150 °C using an Anton Parr thermal attachment. Fitting of the profile, searching the crystal structure and Rietveld refinements were performed by using TOPAS 4.2 [69]. In the determination of thermophysical parameters, the XRD patterns were recorded using the same Bruker D8 ADVANCE powder diffractometer (Cu-Kα radiation) and linear VANTEC detector. The Anton Parr thermal attachment was applied for the temperature control. Nine XRD patterns were measured in the temperature range of 30–270 °C with the 30 °C step and 0.4 s exposition time to obtain the thermal dependences of cell parameters.

All first principal calculations were performed using the density functional theory approach, as implemented in the CASTEP code [70]. The $4f^3\,5s^2\,5p^6\,6s^2$, $3s^2 3p^4$ and $2s^2 2p^4$ valence electron configurations were considered for Pr, S and O atoms, respectively. The local density approximation plus U (LDA + U) based on the Perdew and Zunger parametrization [71] of the numerical results of Ceperley and Alder [72] was used for the calculation. The Hubbard U energy term for the Pr 4f orbital was taken as U_f = 6 eV. The C19 on-the-fly-generated ultrasoft pseudopotentials were used, and the cutoff energy for the plane basis was chosen as that equal to 630 eV. The tolerance level for the geometry optimization was chosen as 5.0×10^{-4} eV/Å for the maximal force and 0.02 GPa for the maximal stress. The Monkhorst-Pack k-point integration network of the Brillouin zone was taken as $3 \times 3 \times 3$.

The particle morphology was observed by Scanning Electron Microscopy (SEM) with the use of an electron microscope JEOL JSM-6510LV. An X-ray energy-dispersive analyzer Oxford Instruments X-Max 20 mm^2 was applied to determine the constituent element ratio. The chemical composition measurements were carried out with the use of a pressed tablet. The accuracy in the element content determination was equal to $\pm 0.2\%$.

The thermal analysis in an argon flow was carried out by a Simultaneous Thermal Analysis (DTA/TG) equipment 499 F5 Jupiter NETZSCH (Germany). The powder sample was inserted into an alumina crucible. The heating rate was 3 °C/min. For the enthalpy determination, the equipment was calibrated with the use of standard substances, such as In, Sn, Bi, Zn, Al, Ag, Au and Ni. The heat effect characteristics were determined with the package Proteus 6 [73]. The peak temperatures and areas in parallel experiments were reproduced with an inaccuracy lower than 3%. The kinetic parameters determination was based on Kissinger formula [74] in the linearized form:

$$\frac{1}{T} = \frac{1}{E} \cdot R \ln \frac{b}{T^2} - \frac{R}{E} \ln \frac{AR}{E}$$

where T is the temperature with the maximum reaction rate; b is the heating rate, dps; E is the activation energy; A is the pre-exponential factor. The examples of the practical application of this formula to the analysis of topochemical reactions in different complex systems can be found elsewhere [35,75–77].

The infrared (IR) absorption spectrum was recorded with a Fourier-transform spectrometer VERTEX 70 V (Bruker, Billerica, MA, USA) in the spectral range from 400 to 1600 cm^{-1} with the spectral resolution of 4 cm^{-1}. The spectrum was recorded for a tablet sample shaped as about 0.4 mm thick tablet of 13 mm in diameter and the weight of 0.1203 g. The tablet was prepared as follows: 0.0030 g of $Pr_2(SO_4)_3$ was thoroughly ground with 0.12 g of KBr. The Globar was used as a light source, and it was equipped with a KBr wide-range beamsplitter (Vilnius, Lithuania) and RT-DLaTGS as a detector.

The Raman experiment with the excitation by a Nd:YAG laser (1064 nm) was carried out on an IR Raman spectrometer (Bruker Optik GmbH), which consists of a Vertex 85 IR spectrometer and a Ram II Raman attachment. The laser output radiation power was as high as 100 mW, and the spectral resolution of the spectrometer was equal to 4 cm^{-1}. The

Raman measurements with the excitation at 532.1 nm were performed using a Millennia solid-state laser (Spectra Physics, Milpitas, CA, USA) and a Trivista 777 triple-grating spectrometer (Princeton Instruments, Trenton, NJ, USA). The Raman spectrum of the $Pr_2(SO_4)_3$ powder was recorded at ambient temperature in the backscattering geometry in the frequency range from 30 to 1400 cm^{-1} without choosing the polarization. The spectral resolution was as high as ~1 cm^{-1}.

For measuring photoluminescence properties, solid samples were filled in spectroscopically pure quartz glass cuvettes and examined either at room temperature or at 77 K (for the latter using a special liquid nitrogen-filled Dewar assembly FL-1013, HORIBA, Singapore). The excitation and emission spectra were recorded with a HORIBA Jobin Yvon Spex Fluorolog 3 spectrometer equipped with a 450 W Xe short-arc lamp, double-grated excitation and emission monochromators, and a photomultiplier tube (R928P) using the FluoroEssence™ software. Both excitation and emission spectra were corrected for the spectral response of the monochromators and the detector using the correction files provided by the manufacturer. The excitation spectra were additionally corrected for the spectral distribution of the lamp intensity by the use of a photodiode reference detector.

3. Results and Discussion

3.1. Structural Properties

The XRD pattern recorded for the $Pr_2(SO_4)_3$ sample is shown in Figure 1a. All reflections were successfully indexed by the C-centered monoclinic cell (a = 21.586, b = 6.715 and c = 6.969 Å, β = 107.93°, GoF = 53.7), and the analysis of reflection extinction showed that the most probable space groups are $C2/c$ or Cc. It should be noted that, earlier, the $Pr_2(SO_4)_3$ structure was indexed by the monoclinic unit cell, but with twice bigger asymmetric unit cell volume (a = 21.71, b = 6.941 and c = 6.722 Å, β = 109.03°, space group $P2/a$) [78]. As far as our unit cell has a higher symmetry and a lower cell volume of asymmetric part, it was chosen for the structure analysis. Moreover, from two possible space groups $C2/c$ and Cc, the former was chosen as a starting point. The crystal structure was solved using a simulated annealing procedure applied to the randomized coordinates of one Pr^{3+} ion and two $(SO_4)^{2-}$ tetrahedra [79]. The dynamic occupancy correction of the atoms was used to merge the ions falling in special positions [79,80]. After the calculations, a solution was found with small R-factors. The crystal structure contains one Pr^{3+} ion in general position (8f), one $(SO_4)^{2-}$ tetrahedron in special site (4e) and one $(SO_4)^{2-}$ tetrahedron in general site (8f), as shown in Figure 2a. The refinement in this model was stable and given the low R-factors, as presented in Table 1 and Figure 1a. The atom coordinates and main bond lengths are given in Tables S1 and S2, respectively. The structural analysis of $Pr_2(SO_4)_3$ with the use of program PLATON [81] does not reveal any additional elements of symmetry, and it proves the selection of space group $C2/c$.

The bond valence sum calculated for the Pr^{3+} ion using values r_0 = 2.138 Å and b_0 = 0.37 [82] and taking into account short bond lengths d(Pr–O) in the range of 2.349(5)–2.530(7) Å without long bond lengths (2.716(7)–2.792(8) Å) gave the value BVS(Pr^{3+}) = 3.11, which is close to the formal valence state 3+ of the Pr ion. Similar calculations for all S^{6+} ions were made using r_0 = 1.624 Å, b_0 = 0.37 [75] yield BVS(S1) = 5.71 and BVS(S2) = 6.52, which are also in a good agreement (less than ±10% of average value) with the formal valence state 6+ of S ions. Thus, accounting for short bond lengths d(Pr–O), one can assume the existence of monocaped trigonal PrO_7 prisms in the structure (Figure 2a). These prisms are joined with SO_4^{2-} tetrahedra by nodes forming a 3D net. The topological analysis of the net, using the simplification that $S1O_4$, $S2O_4$ and PrO_7 are just nodes, reveals that this is a three-nodal (4-c)(5-c)$_2$(9-c)$_2$ net with the point symbol $(3^2.4^2.5^2)(3^2.4^7.5)_2(3^6.4^{14}.5^8.6^8)_2$, which is new [83]. Thus, presently, this family of monoclinic anhydrous sulfates includes three compounds $Ln_2(SO_4)_3$ (Ln = Pr, Nd, Eu), for which structural parameters are known [42,43]. However, with a high probability, it can be assumed that $Ln_2(SO_4)_3$ (Ln = Pm, Sm) have structures of the same type.
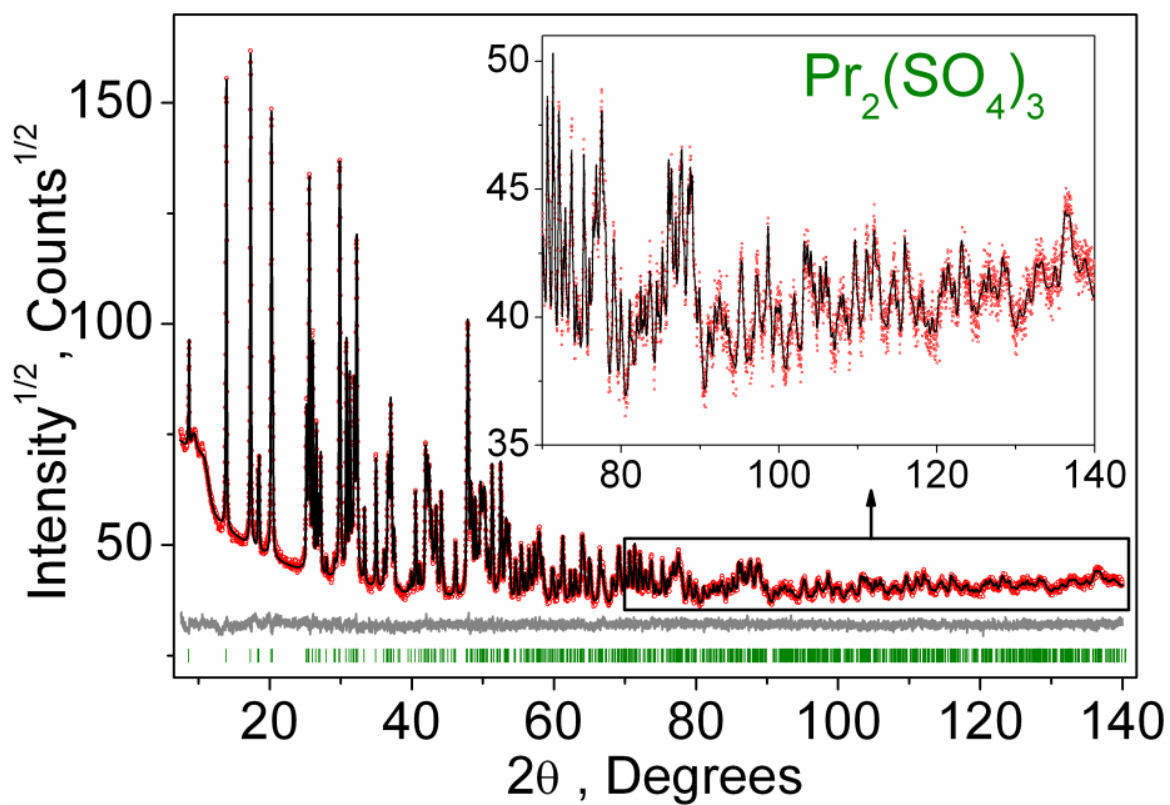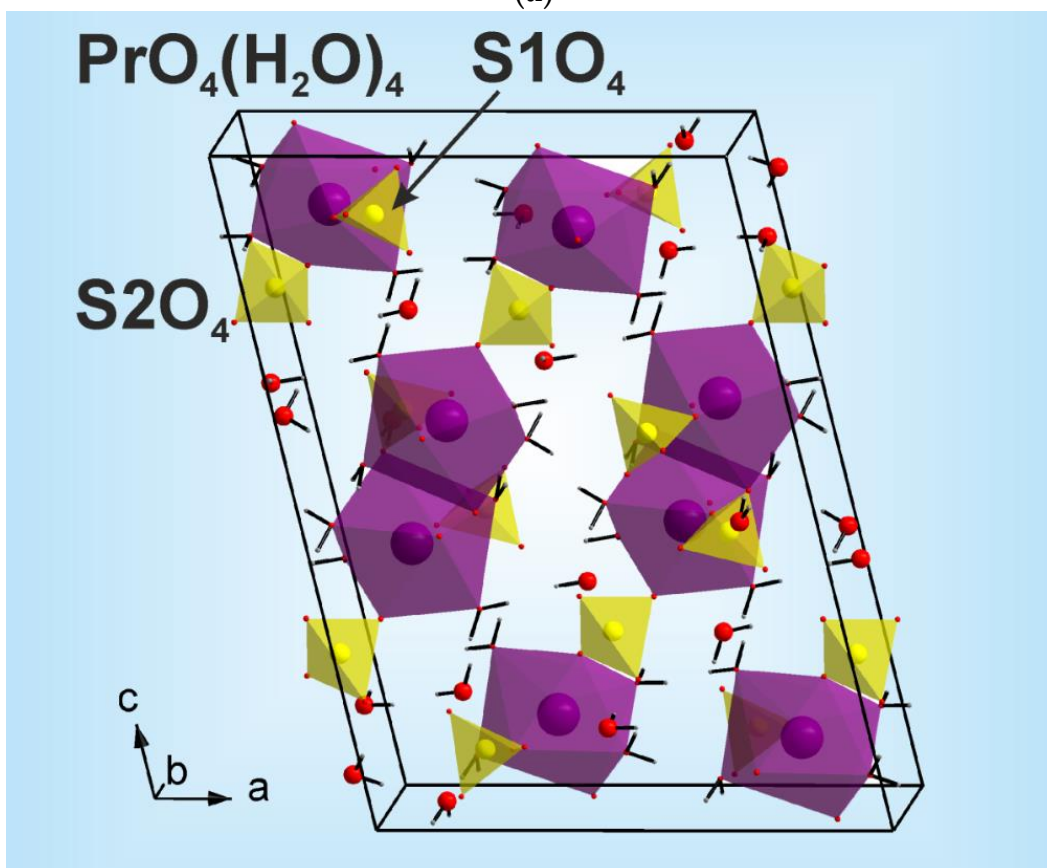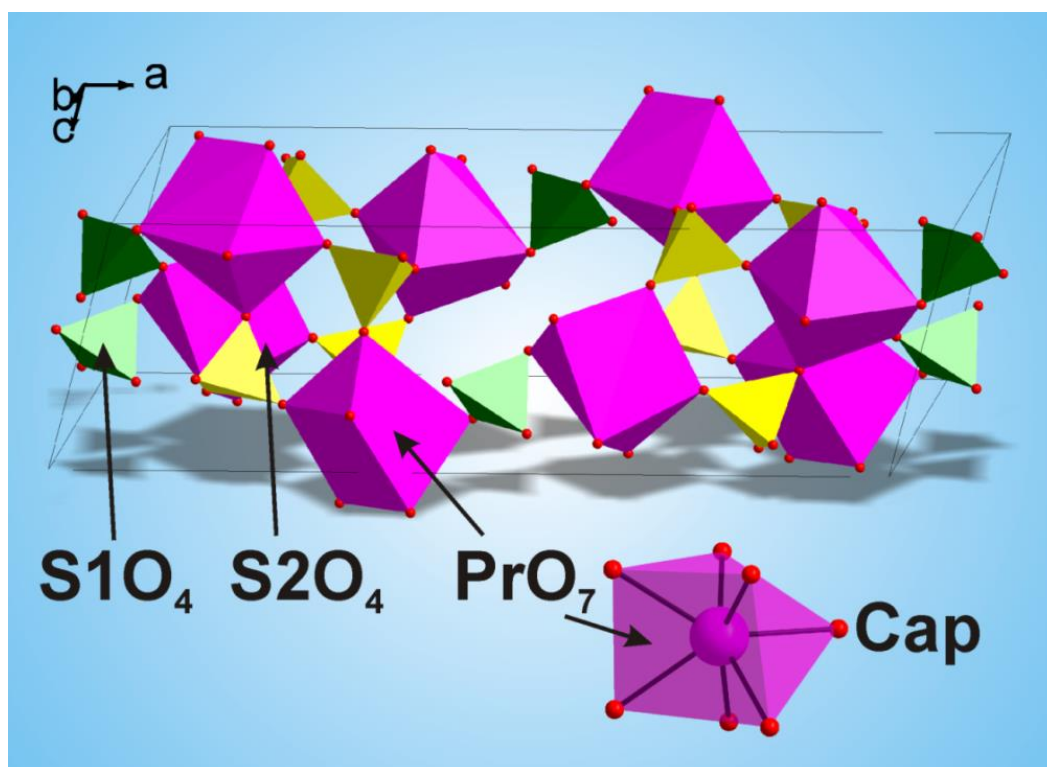
(**a**)
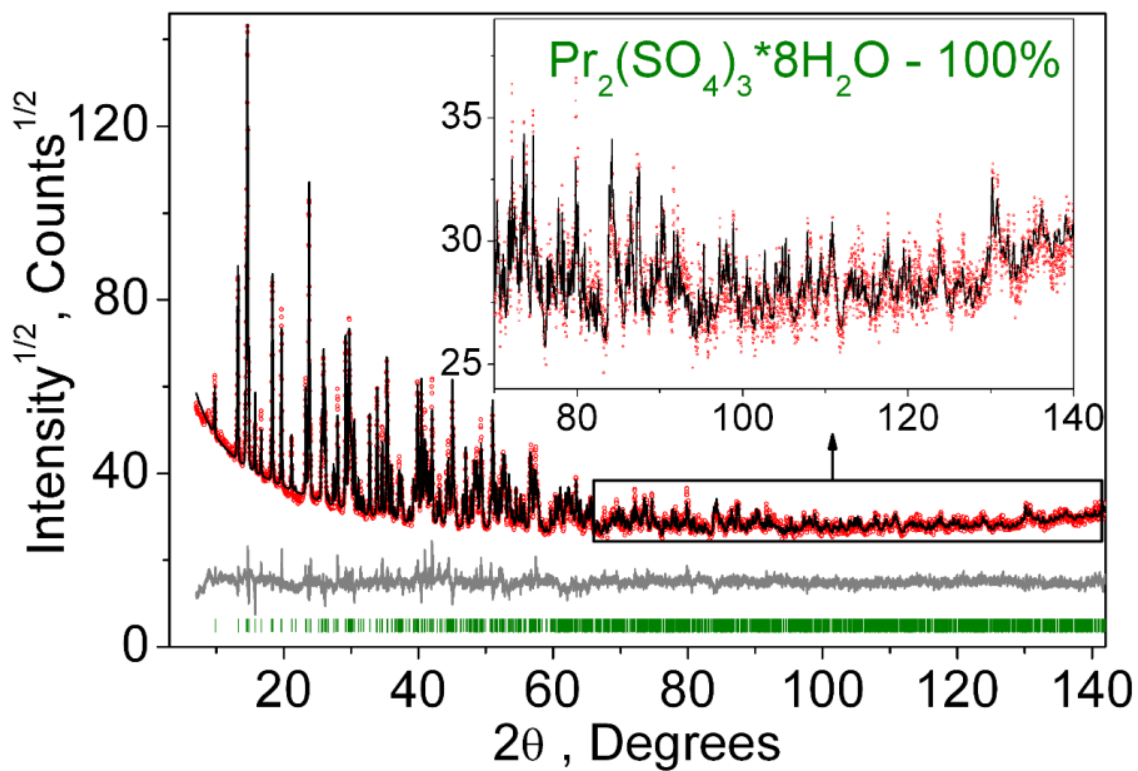
(**b**)

Figure 1. XRD patterns and difference Rietveld plots of (**a**) $Pr_2(SO_4)_3$, as obtained at 150 °C, and (**b**) $Pr_2(SO_4)_3 \cdot 8H_2O$.

(**a**)

(**b**)

Figure 2. Crystal structures of (**a**) $Pr_2(SO_4)_3$ and (**b**) $Pr_2(SO_4)_3 \cdot 8H_2O$. The unit cell is outlined. Lone atoms are omitted for clarity.

**Table 1.** Main parameters of processing and refinement of the $Pr_2(SO_4)_3$ sample.

Compound	$Pr_2(SO_4)_3$
Space group	*C2/c*
a, Å	21.6052 (4)
b, Å	6.7237 (1)
c, Å	6.9777 (1)
β, °	107.9148 (7)
V, Å^3	964.48 (3)
Z	4
2θ-interval, °	7.5–140
T_{meas}.	150 °C
Number of reflections	922
Number of refined parameters	71
R_{wp}, %	2.75
R_p, %	2.16
R_{exp}, %	2.10
χ^2	1.31
R_B, %	0.69

As seen in Figure 3, heating the $Pr_2(SO_4)_3$ sample from 30 to 270 °C leads to an increase of all cell parameters (Table S3) with δa~0.23%, δb~0.15% and δc~0.39%, showing the 3D net expansion in all crystallographic directions accompanied by an increase of the monoclinic angle β. The continuous variation of the cell parameters (Figure 3) and freedom from the reflection splitting and/or superstructure reflections in the powder patterns (Figure S3) indicate the absence of structural phase transitions in the range of 30–270 °C. Therefore, we can suggest that $Pr_2(SO_4)_3$ at room temperature also adapts the *C2/c* space group. The thermal expansion tensor of $Pr_2(SO_4)_3$ is shown in Figure 4. As is evident, the crystal expansion is strongly anisotropic. Moreover, there is a direction along which a contraction appears on heating, mainly due to a monoclinic angle increase.

Figure 3. *Cont.*

(e)
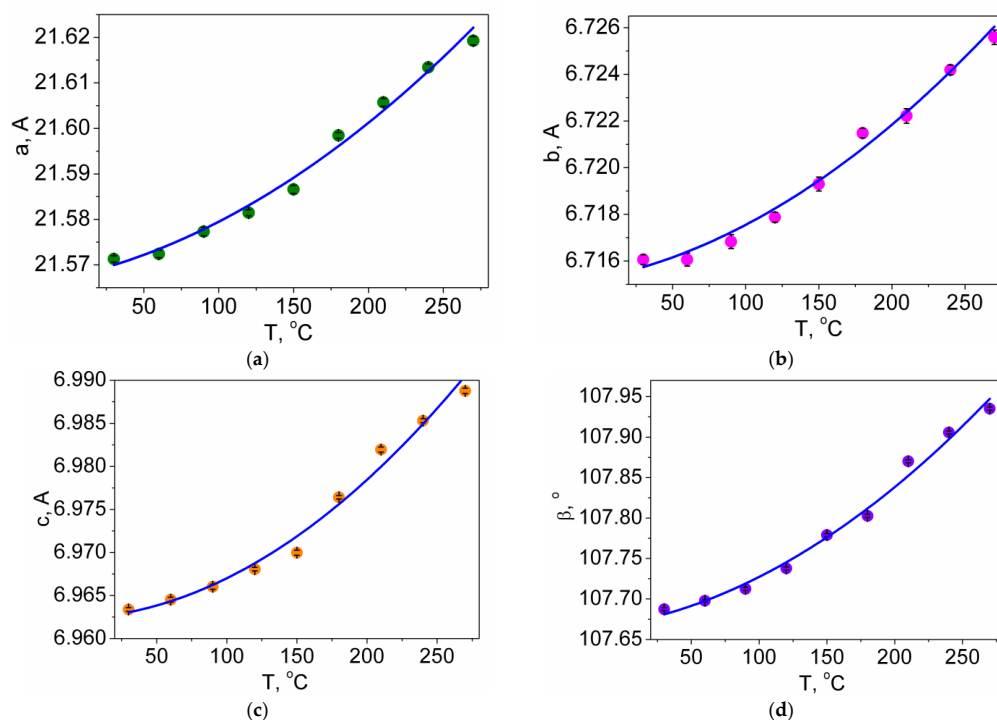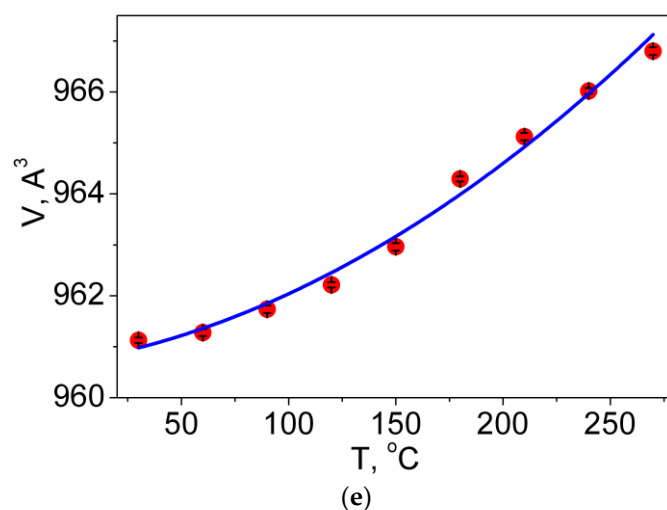
Figure 3. Thermal dependence of $Pr_2(SO_4)_3$ cell parameters: (**a**) a(T); (**b**) b(T); (**c**) c(T); (**d**) β(T); (**e**) V(T).
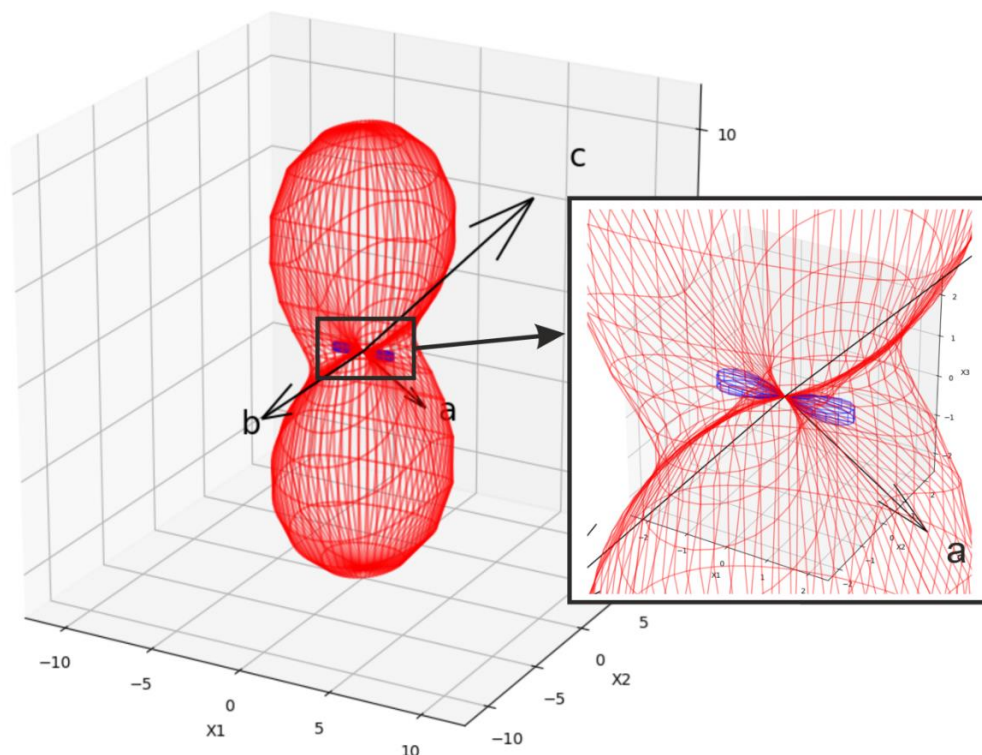
Figure 4. Thermal expansion tensor of $Pr_2(SO_4)_3$ calculated for the temperature range of 30–150 °C. Contraction is shown in blue color.

The XRD pattern recorded for the $Pr_2(SO_4)_3·8H_2O$ sample is shown in Figure 1b. All peaks of the pattern were indexed according to the known structure of $Pr_2(SO_4)_3·8H_2O$ [23], and, therefore, this structure was used as the initial model. The refinements were stable and gave low R-factors, as listed in Table 2 and shown in Figure 1b. The atom coordinates and main bond lengths are in Tables S4 and S5, respectively. Hydrogen atoms were placed in ideal sites and their coordinates were fixed during a further crystal structure refinement. The asymmetric part of the unit cell contains one Pr ion, two S ions, six O ions and four H_2O molecules. The Pr^{3+} ion is coordinated by four O ions and four H_2O molecules forming a $PrO_4(H_2O)_4$ antisquare prism. Each S ion is coordinated by four O ions forming a SO_4

tetrahedra. The SO_4 tetrahedra are linked with $PrO_4(H_2O)_4$ polyhedra by edges and nodes forming a 3D net, as displayed in Figure 2b.

Table 2. Main parameters of processing and refinement of the $Pr_2(SO_4)_3 \cdot 8H_2O$ sample.

Compound	$Pr_2(SO_4)_3 \cdot 8H_2O$
Space group	$C2/c$
a, Å	13.7058 (2)
b, Å	6.8664 (1)
c, Å	18.4702 (3)
β, °	102.816 (1)
V, Å^3	1694.91 (5)
Z	4
2θ-interval, °	7–144
$T_{meas.}$	24 °C
Number of reflections	1689
Number of refined parameters	48
R_{wp}, %	6.63
R_p, %	5.08
R_{exp}, %	2.95
χ^2	2.24
R_B, %	3.65

The crystallographic data of the crystal structures of $Pr_2(SO_4)_3$ and $Pr_2(SO_4)_3 \cdot 8H_2O$ are deposited in Cambridge Crystallographic Data Centre (CSD #2167673-2167674). The data can be down loaded from the site (www.ccdc.cam.ac.uk/data/request/cif, accessed on 20 April 2022).

3.2. Electronic Properties

The Brillouin zone (BZ) image and the calculated electronic band structure of $Pr_2(SO_4)_3$ are shown in Figures 5 and S4, respectively. The paths along high symmetry points of the BZ are selected as follows: Γ–C, C_2–Y_2–Γ–M_2–D, D_2–A–Γ, L_2–Γ–V and the coordinates of these points are: Γ(0,0,0), C(−0.277, 0.277,0), C_2(−0.723, −0.277, 0), Y_2(−0.5, −0.5, 0), M_2(−0.5, −0.5, 0.5), D(−0.749, −0.251, 0.5), D_2(−0.251, 0.251, 0.5), A(0, 0, 0.5), L_2(−0.5, 0, 0.5), V_2(−0.5, 0, 0). As praseodymium is related to lanthanides, the spin up and spin down band structures were calculated. According to the results shown in Figure 5, $Pr_2(SO_4)_3$ is a direct band gap compound. The valence band maximum (VBM) and conduction band minimum (CBM) are located in the center of BZ. The calculated spin up band gap is equal to 5.47 eV, while the spin down band gap is as high as 5.69 eV. It should be noted that flat narrow electronic branches are observed at 2.78–3.01 eV in a spin up band structure and at 4.89–5.42 eV in a spin down band structure. To understand the nature of these branches and the nature of band gap, the partial density of electronic states is presented in Figure 6. From the curve observation, it can be concluded that the flat branches pointed above are formed by the f electronic states of Pr. The valence band top is dominated by the p electrons of oxygen ions, while the conduction band bottom is formed by the d electrons of Pr^{3+} ions.

3.3. Vibrational Properties

There are 34 atoms in the primitive cell of $Pr_2(SO_4)_3$ and the symmetry analysis leads to the following distribution of the 102 phonon modes between the irreducible representations at the center of Brillouin zone: $\Gamma_{vibr} = 25A_g + 25A_u + 26B_g + 26B_u$ where acoustic modes are $\Gamma_{acoustic} = A_u + 2B_u$, and the remaining modes are optical. The g-labeled modes are Raman active, while the u-labeled modes are infrared active [84]. The vibrational spectra obtained for powder $Pr_2(SO_4)_3$ are presented in Figure 7. The comparison of the Raman spectra recorded with the use of 1064 and 532.1 nm laser wavelengths is shown in Figure S5 and excellent relation of the spectra is evident. Thus, the luminescence lines do not appear under the excitation at 1064 and 532.1 nm and both wavelengths can be used for precise measurements of the Raman spectra of Pr^{3+}-containing crystals. In the $Pr_2(SO_4)_3$ structure,

the SO_4 tetrahedra occupy two crystallographically independent positions, namely, C_1 and C_2. As is known, free $[SO_4]^{2-}$ units have the T_d symmetry, and the characteristic wavenumbers of normal vibrations of this ion group were listed in [85]. The correlation between internal vibrations of the free SO_4 tetrahedra with the T_d symmetry, sites symmetry and factor group symmetry of the unit cell is shown in Table 3. Herein, the mode ν_1 (A_1) is symmetric stretching vibration, ν_3 (F_2) is antisymmetric stretching vibration and ν_2 (E) and ν_4 (F_2) are symmetric and antisymmetric bending vibrations. The shapes of the vibrational spectra of $Pr_2(SO_4)_3$ and $Eu_2(SO_4)_3$ [43] powders are quite similar. This can be explained by the fact that the structures of these compounds are described in the same space groups and have the same number of SO_4 tetrahedra in the same positions. However, due the differences in $[SO_4]^{2-}$ bond lengths, there is a slight shift in the spectral peaks, which is especially clear in the range of ν_1 vibrations, as shown in Figure S6.
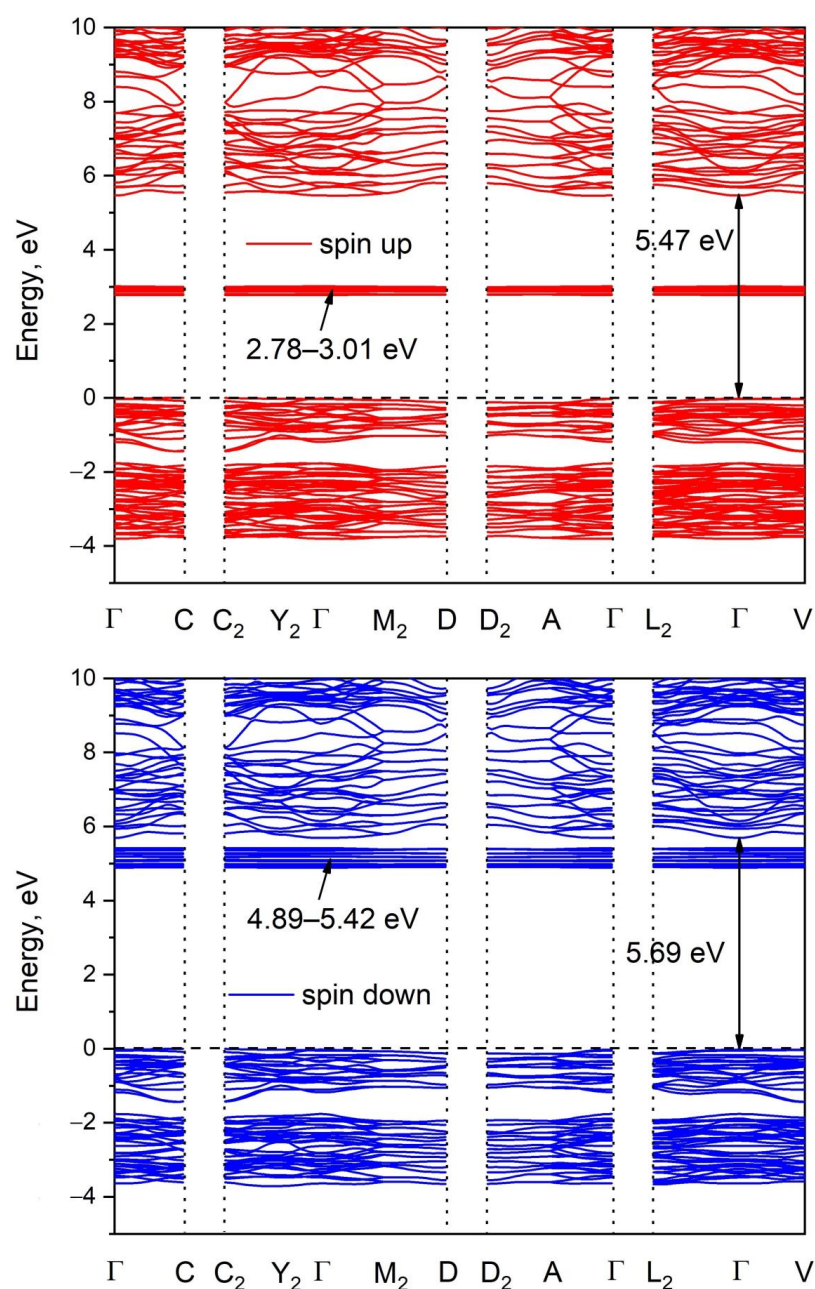
Figure 5. Calculated band structure of $Pr_2(SO_4)_3$. The lower panel is for spin up and the upper panel is for spin down.
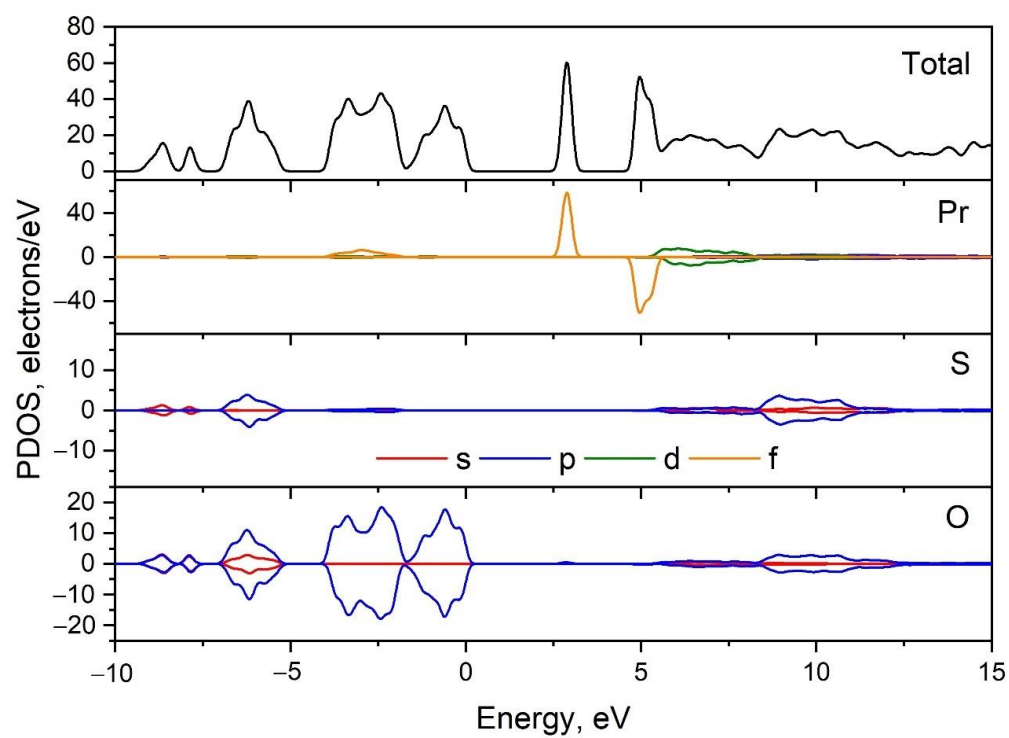
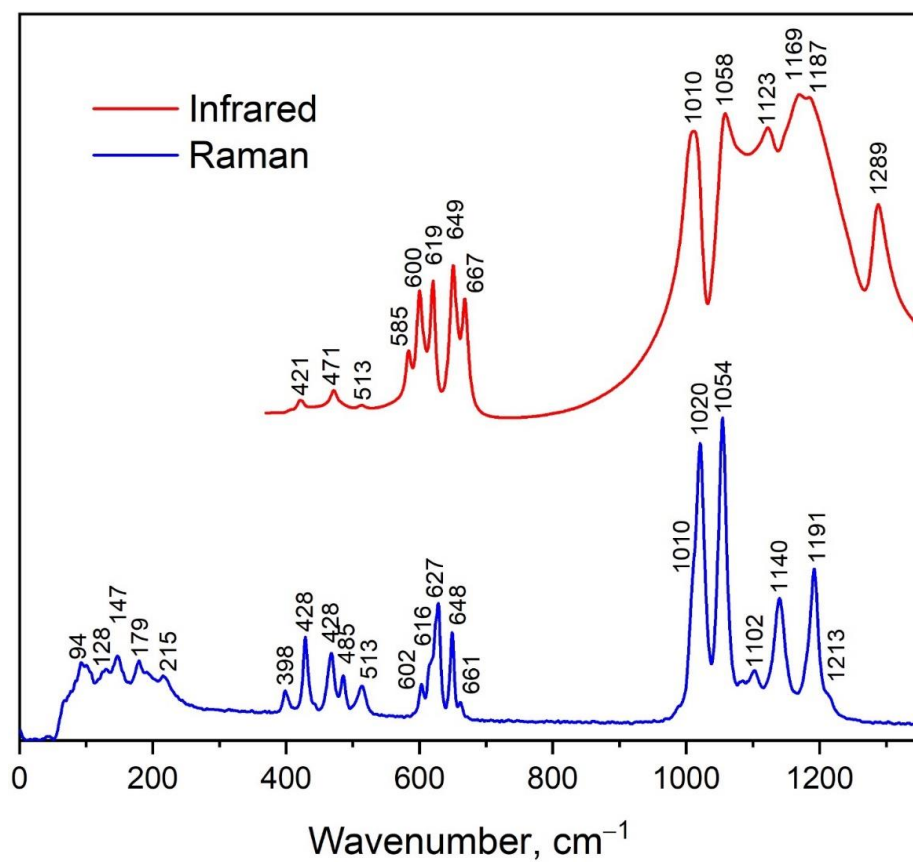**Figure 6.** Calculated partial density of states in $Pr_2(SO_4)_3$.

Figure 7. Raman and infrared spectra of $Pr_2(SO_4)_3$.

Table 3. Correlation scheme for the SO_4^{2-} ion placed into the C_1 and C_2 symmetry positions of the unit cell having C_{2h} symmetry.

Wavenumber, cm^{-1} [81]	T_d Free Molecule Symmetry	C_1 Site Symmetry	C_{2h} Unit Cell Symmetry
983	A_1 (ν_1)	A	$A_g + A_u + B_g + B_u$
450	E (ν_2)	$2A$	$2A_g + 2A_u + 2B_g + 2B_u$
1105	F_2 (ν_3)	$3A$	$3A_g + 3A_u + 3B_g + 3B_u$
611	F_2 (ν_4)	$3A$	$3A_g + 3A_u + 3B_g + 3B_u$
	T_d Free molecule symmetry	C_2 Site symmetry	C_{2h} Unit cell symmetry
983	A_1 (ν_1)	A	$A_g + A_u$
450	E (ν_2)	$2A$	$2A_g + 2A_u$
1105	F_2 (ν_3)	$A + 2B$	$A_g + A_u + 2B_g + 2B_u$
611	F_2 (ν_4)	$A + 2B$	$A_g + A_u + 2B_g + 2B_u$

According to Table 3, the high wavenumber part (above 950 cm^{-1}) of Raman and infrared spectra of $Pr_2(SO_4)_3$ powder is correspondent to the stretching vibrations of SO_4^{2-} ions. The spectral bands related to each symmetric stretching vibration of SO_4 are clearly seen in the Raman spectrum at 1010, 1020 and 1054 cm^{-1}, as seen in Figures 7 and S7. The remaining Raman bands in this region are attributed to antisymmetric stretching vibrations. The broad band observed at 1010 cm^{-1} in the infrared spectrum should consist of three overlapped bands corresponding to ν_1 vibrational modes, and the bands above 1030 cm^{-1} are related to antisymmetric stretching vibrations. The ν_4 vibrations are located in the range of 595–670 and 575–675 cm^{-1} in Raman and infrared spectra, respectively (Figures 7 and S8). The ν_2 modes are observed in the Raman spectrum between 380 and 520 cm^{-1}. Other Raman bands revealed below 250 cm^{-1} attributed to the rotation of SO_4^{2-} and translational vibrations of the structural units. Thus, we can say that positions of spectral bands and their number are in agreement with group-theoretical analysis data for the $Pr_2(SO_4)_3$ XRD-solved structure.

The calculated partial phonon density of states is shown in Figure 8 and the presented data can be summarized as follows: the vibrations of SO_4 tetrahedra dominated in the Raman and infrared spectra at wavenumbers above 250 cm^{-1}, while the low wavenumber region is characterized by vibrations of all kinds of ions.

3.4. Thermal Properties

The known problem with sulfates is their increased hygroscopicity. Upon obtaining functional materials based on lanthanide sulfates, important issues are the processes occurring during the dehydration of the corresponding salts. Pyrohydrolysis, often proceeding during the dehydration of salts, can significantly affect the properties of sulfate materials. In this relation, the TG/DTA data of praseodymium sulfate octahydrate were recorded on heating in the temperature range of 25–1400 °C in the argon atmosphere, as shown in Figure 9. According to the TG data in the temperature range of 73–210 °C, the mass loss is 20.2%, which allows us to draw up the process equation:

$$Pr_2(SO_4)_3 \times 8H_2O \rightarrow Pr_2(SO_4)_3 + 8H_2O \qquad (3)$$
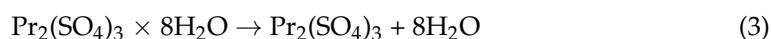
The dehydration proceeds in one stage despite the crystallo-chemical inequality of water molecules entering the structure [86]. In the interval of 350–370 °C, in all recorded DTA curves, a low-intensity peak of heat release was detected. To identify the source of this effect, isothermal treatments of praseodymium sulfate octahydrate were carried out at 250 °C and 350 °C. In both cases, the mass loss corresponds to the full dehydration of the samples. According to the X-ray phase analysis and electron microscopy, the starting octahydrate is represented by highly faceted crystals ranging in size from 5 to 20 µm

(Figure 10a). Heating the $Pr_2(SO_4)_3 \times 8H_2O$ sample to 250 °C results in the formation of an X-ray amorphous product obtained by the dehydration process (Figure 10b). Obviously, the water vapor moving to the surface results in the particle destruction. The sample heating to 350 °C results in a polycrystalline powder of anhydrous $Pr_2(SO_4)_3$ (Figure 10c), which was obviously formed via the recrystallization of the amorphous powder obtained at the initial stage of dehydration. Therefore, the presence of the heat release peak on the DTA curve is caused by the crystallization of the amorphous phase of $Pr_2(SO_4)_3$.
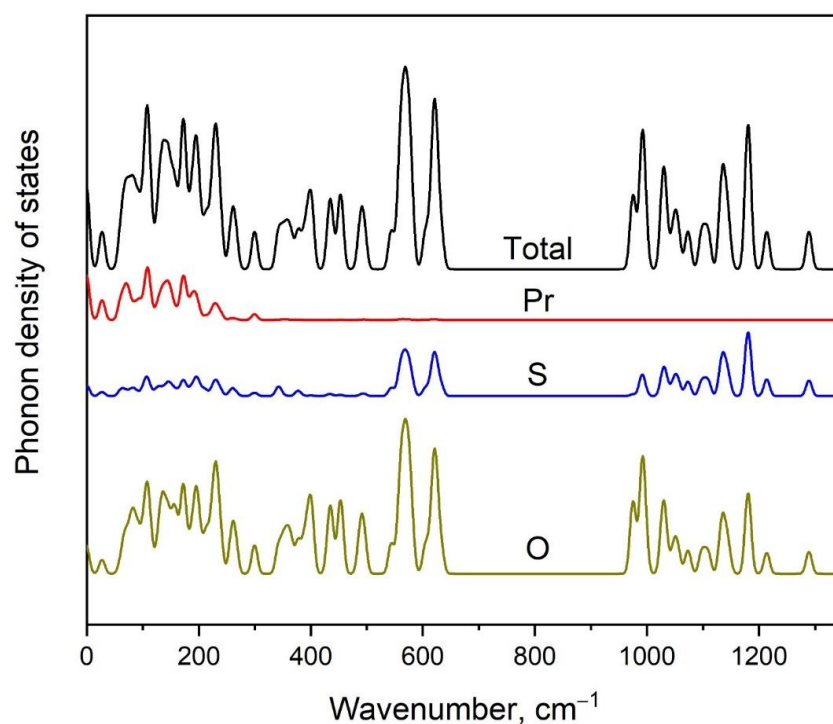
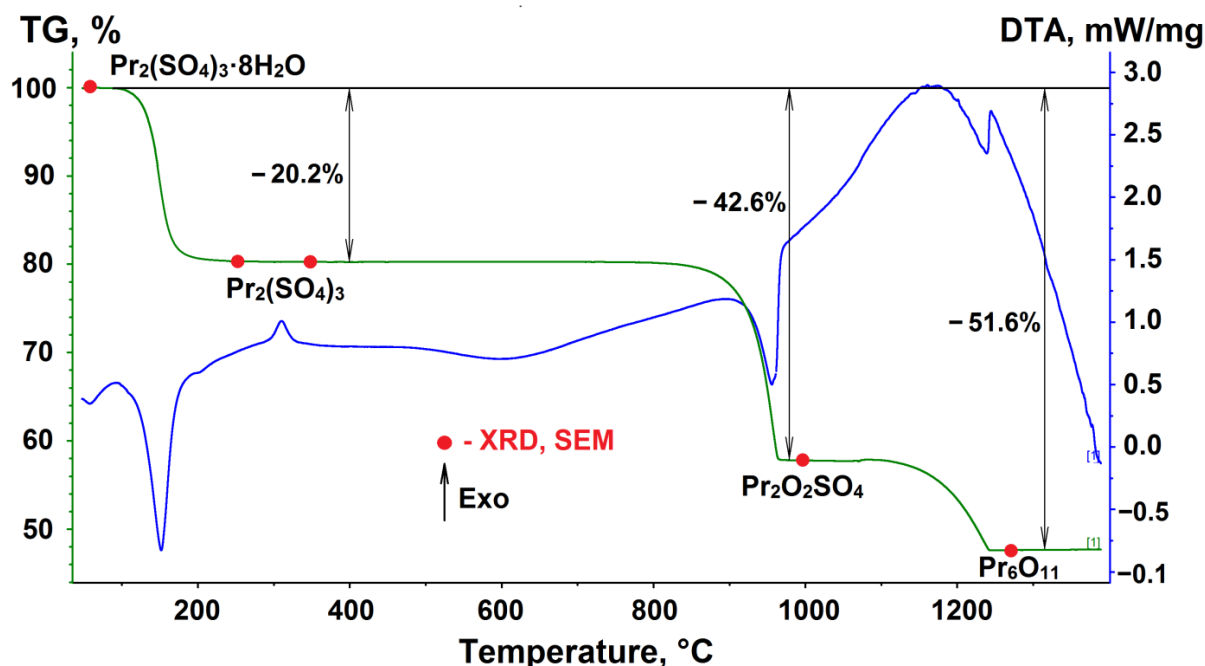**Figure 8.** Calculated phonon density of states in $Pr_2(SO_4)_3$.

Figure 9. Simultaneous DTA/TG of $Pr_2(SO_4)_3$.
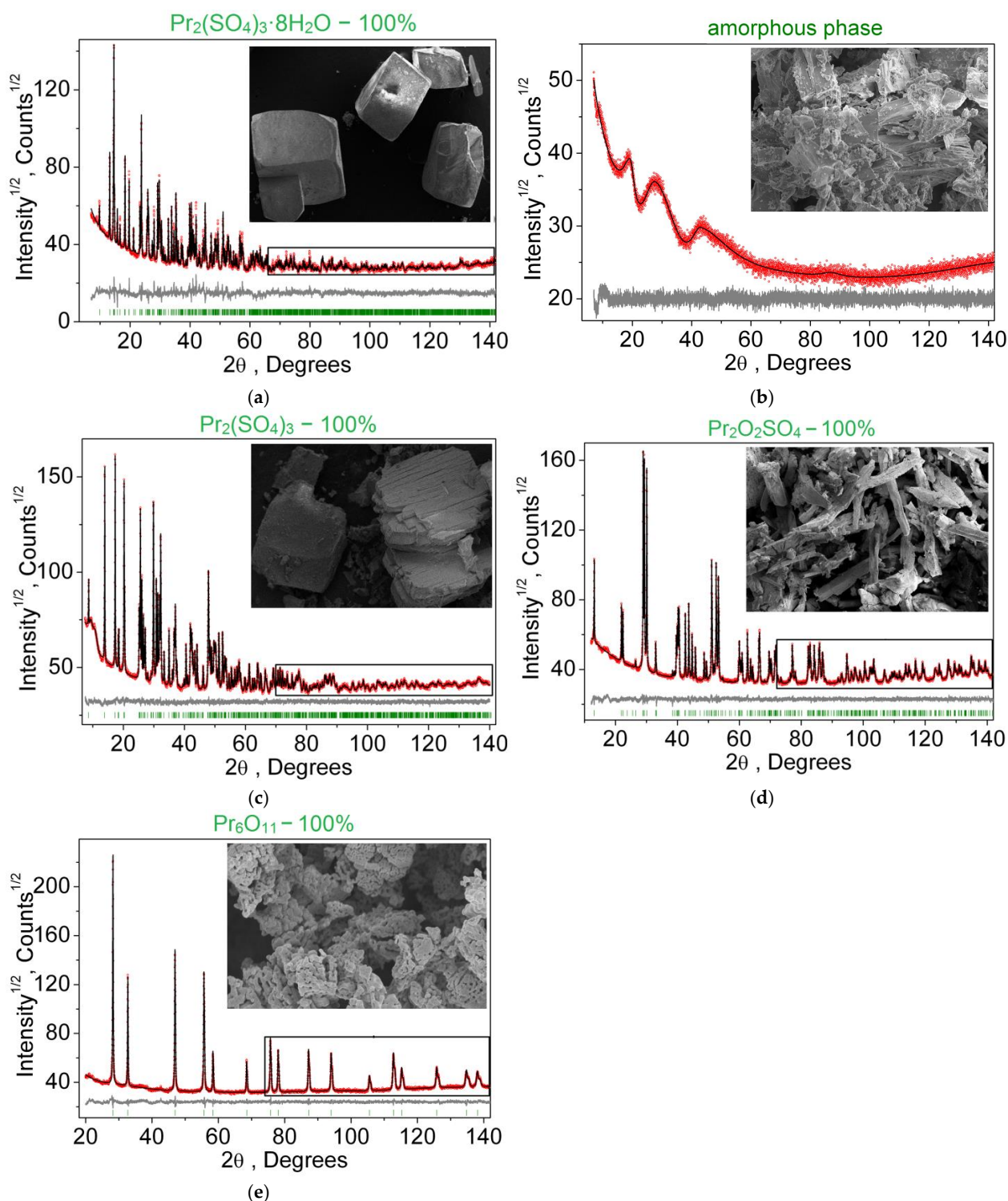
Figure 10. Difference Rietveld plots and microstructure transformation of polycrystalline samples $Pr_2(SO_4)_3 \cdot 8H_2O$ subjected to heat treatment at temperatures: (**a**) 25 °C (room temperature); (**b**) 250 °C; (**c**) 350 °C; (**d**) 1000 °C; (**e**) 1270 °C.

Further decomposition of $Pr_2(SO_4)_3$ on heating occurs in two steps. In the first step, in the temperature range of 850–970 °C, two sulfate groups undergo decomposition, resulting in the formation of praseodymium oxysulfate (Figure 10d):

$$Pr_2(SO_4)_3 \rightarrow Pr_2O_2SO_4 + 2SO_2 + O_2 \tag{4}$$
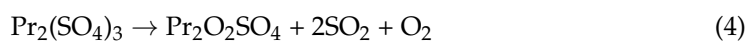
In the second step, in the temperature range 1100–1250 °C, the remaining sulfate groups were decomposed. According to the X-ray phase analysis, a mixed praseodymium oxide Pr_6O_{11} is formed (Figure 10e) as the final product of the reaction:

$$6Pr_2O_2SO_4 \rightarrow 2Pr_6O_{11} + 6SO_2 + O_2 \qquad (5)$$
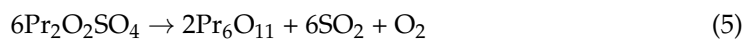
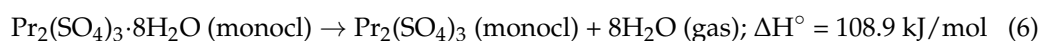The formation of intermediate oxide Pr_6O_{11} is characteristic of the decomposition of oxygen-containing praseodymium compounds, just as the formation of CeO_2 is typical of the corresponding cerium compounds [87] and Tb_4O_7 for terbium [88]. $4f$-electron shell structures enhance the effect on the thermodynamic characteristics of compounds while simplifying the chemical composition.

On the base of reliable data on the phase composition of the compounds formed by thermal transformations, as well as the established values of the enthalpies of these transformations, we can write the thermochemical equations of the processes related to the $Pr_2(SO_4)_3 \cdot 8H_2O$ decomposition on heating:

$$Pr_2(SO_4)_3 \cdot 8H_2O \text{ (monocl)} \rightarrow Pr_2(SO_4)_3 \text{ (monocl)} + 8H_2O \text{ (gas)}; \Delta H° = 108.9 \text{ kJ/mol} \quad (6)$$

$$Pr_2(SO_4)_3 \text{ (monocl)} \rightarrow Pr_2O_2SO_4 \text{ (monocl)} + 2SO_2(gas) + O_2 \text{ (gas)}; \Delta H° = 499.8 \text{ kJ/mol} \qquad (7)$$

$$6Pr_2O_2SO_4 \text{ (monocl)} \rightarrow 2Pr_6O_{11} \text{ (cub)} + 6SO_2(gas) + O_2 \text{ (gas)}; \Delta H° = 245.5 \text{ kJ/mol} \quad (8)$$

Using the data on the formation enthalpies of binary compounds Pr_6O_{11} [89], SO_2 [90] and H_2O [91], the enthalpies of praseodymium sulfates formation (Table 4) were successively calculated: $Pr_2O_2SO_4$ (according to reaction (8)), $Pr_2(SO_4)_3$ (according to reaction (7)) and $Pr_2(SO_4)_3 \cdot 8H_2O$ (according to reaction (6)).

Table 4. Standard enthalpies of praseodymium sulfate formation.

Compound	$\Delta H°f$, kJ/mol
$Pr_2(SO_4)_3 \cdot 8H_2O$	−5361.2
$Pr_2(SO_4)_3$	−3317.9
$Pr_2O_2SO_4$	−2224.3

To study the kinetics of the thermal decomposition processes of $Pr_2(SO_4)_3 \cdot 8H_2O$, the sample thermal analysis was carried out at different heating rates: 3, 5, 10 and 15 °C/min. Based on the DTA data obtained at different heating rates (Figures S9 and S10), the kinetic parameters of the processes were calculated (Table 5). As can be seen, the increase in the activation energy during the transition from the dehydration process to the processes of sulfate decomposition is somewhat compensated by the increase in the pre-exponential factor value, which actually reflects the increase in the favorable steric factor. In general, in accordance with a significant expansion of the peaks in the DTA curves and, accordingly, with a significant increase in the activation energy of high-temperature processes for the decomposition of sulfate $Pr_2(SO_4)_3$ and oxysulfate $Pr_2O_2SO_4$, we can note their significant kinetic complexity, compared with the dehydration of crystalline hydrate $Pr_2(SO_4)_3 \cdot 8H_2O$.

Table 5. Kinetic parameters of the decomposition of praseodymium sulfates.

| Number of Reaction	Chemical Equation	A	E_a, kJ/mol
1	$Pr_2(SO_4)_3 \cdot 8H_2O \rightarrow Pr_2(SO_4)_3 + 8H_2O$	6×10^6	77
2	$Pr_2(SO_4)_3 \rightarrow Pr_2O_2SO_4 + 2SO_2 + O_2$	1×10^{10}	303
3	$6Pr_2O_2SO_4 \rightarrow 2Pr_6O_{11} + 6SO_2 + O_2$	2×10^8	323

A comparison of the thermal decomposition of praseodymium sulfate octahydrate with the corresponding crystalline hydrate of europium sulfate $Pr_2(SO_4)_3 \cdot 8H_2O$ indicates a

greater kinetic stability of $Pr_2(SO_4)_3 \cdot 8H_2O$ and $Pr_2(SO_4)_3$, compared with the corresponding europium compounds, and a reduced stability of $Pr_2O_2SO_4$ compared to $Eu_2O_2SO_4$ [92]. This fact has, obviously, energetic reasons and is in a good agreement with the enthalpies of compound formation.

3.5. Luminescent Properties

Under the excitation at 450 nm, $Pr_2(SO_4)_3$ exhibits modest luminescence in the red well seen through the filter, with the intensity typical of concentrated rare-earth-containing nonabsorbing materials. The photoluminescence emission spectra excited at the $^3P_2 \leftarrow {}^3H_6$ transition at 440 nm recorded at room temperature (blue line) and at 77 K (red line), are presented in Figure 11. Both emission spectra are dominated by the $^3P_0 \rightarrow {}^3F_2$ transition with a maximum at 640 nm. The Pr^{3+} ion luminescence in the visible spectral range is expected to include the contributions mainly from $^3P_0$ and $^1D_2$ excited states, since $^3P_2$, commonly, nonradiatively relaxes to $^3P_0$, and in the hosts with a large phonon cutoff frequency, a considerable probability of nonradiative population of $^1D_2$ level is assumed. Despite only two luminescent energetic states, the emission spectra of the Pr^{3+} ion are featured by overlapping bands terminating at different low-lying excited states. Another feature is the variability of the intensity distribution over the luminescence bands via the change of crystal field acting onto the Pr^{3+} ion in different hosts, or more specifically, by the change of oscillator strengths and energies of both starting and terminating levels. For example, either $^1D_2 \rightarrow {}^3H_4$ or $^3P_0 \rightarrow {}^3H_6$ or $^3P_0 \rightarrow {}^3F_2$ could be a maximal in different hosts under the excitation via ^3P_J. Therefore, the assignment of the Pr^{3+} luminescence bands must be made very carefully in contrast to Eu^{3+}, for instance. Figure 12 shows the 77 K excitation spectrum of $Pr_2(SO_4)_3$ monitored at 640 nm (magenta) and the neighboring part of emission spectrum (blue). Peak at 480 nm (20,833 cm^{-1}) must be associated with the zero phonon line (ZPL) of the $^3P_0 \leftarrow {}^3H_4$ transition, and the weak sideband at longer wavelengths then must be a contribution of thermally distributed phonons corresponding to 77 K. The corresponding peak in the emission spectrum is shifted to longer wavelengths by the ZPL width that can be explained by the reabsorption of emitted radiation within the ZPL width. The longer-wavelength spectral structure in the emission spectrum (in the range 484–500 nm) then must be assigned to the phonon sideband that, in contrast to the excitation process, must not obey the thermal distribution of phonons and is limited by the vibrational spectrum of the local environment of praseodymium ion. Peculiarly, the reabsorption effect for the spectral distribution of luminescence in $Pr_2(SO_4)_3$ is weaker than that in another self-activated crystal $PrAlGe_2O_7$ [93], where the disappearance of $^3P_0 \rightarrow {}^3H_4$ and $^1D_2 \rightarrow {}^3H_4$ spectral features, with respect to the Pr-doped $LaAlGe_2O_7$ crystal, was observed. One more peculiarity is the absence of the $^3P_0 \rightarrow {}^3F_3$ line that is completely unobservable at the background of the $^3P_1 \rightarrow {}^3F_4$ band. This latter effect cannot be related to the reabsorption; however, it must be associated with a certain dependence of the intensity of this line on the crystal field, like it has been recently observed in [94].

After determining the $^3P_0$ ZPL position, the assignment of most bands shown in Figure 11 is rather straightforward and becomes consistent with the consideration by Srivastava [95]. Both room temperature and 77K emission spectra are dominated by the luminescence at the $^3P_0 \rightarrow {}^3F_2$ transition peaking at 640 nm. The spectral region in the vicinity of 600 nm contains contributions from two possible channels, namely, from $^3P_0 \rightarrow {}^3H_6$ and $^1D_2 \rightarrow {}^3H_4$. The band peaking at 525 nm is very weak at 77 K and gains more intensity at room temperature; therefore, it must be ascribed to the emission from the thermally populated $^3P_1$ level to $^3H_5$. The same behavior reveals the origin of the bands at 675 and 700 nm that are the emissive transitions $^3P_1 \rightarrow {}^3F_{3,4}$.
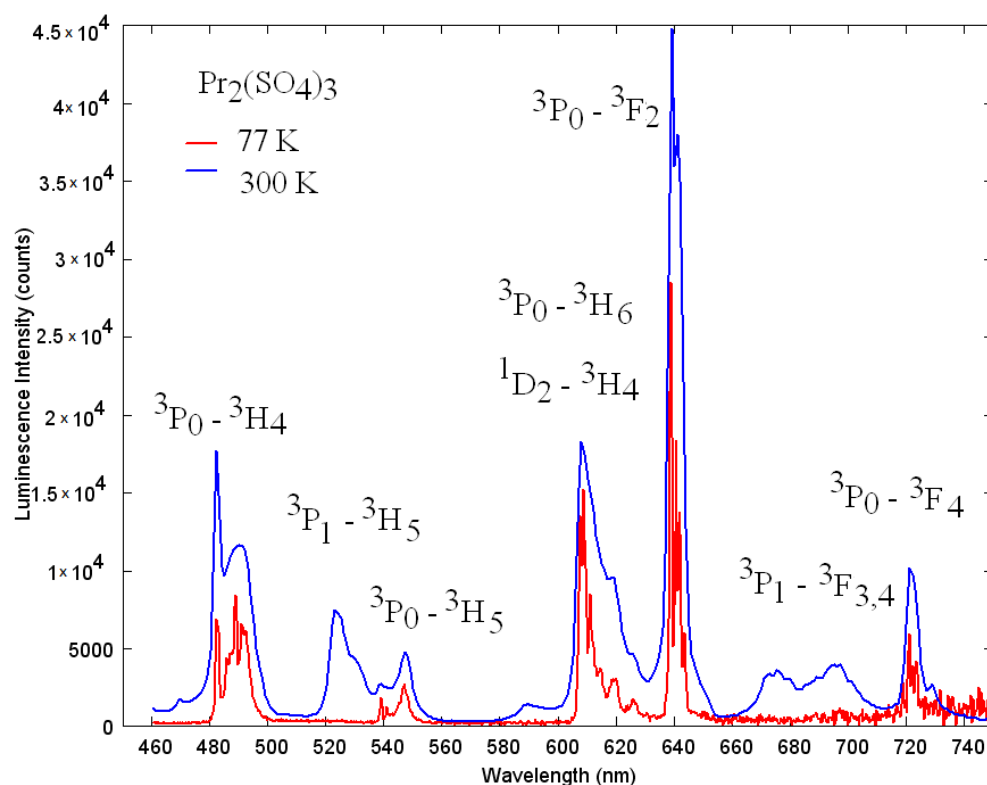
Figure 11. High resolution emission spectra of $Pr_2(SO_4)_3$ at room temperature (blue) and at 77 K (red) excited at 440 nm.
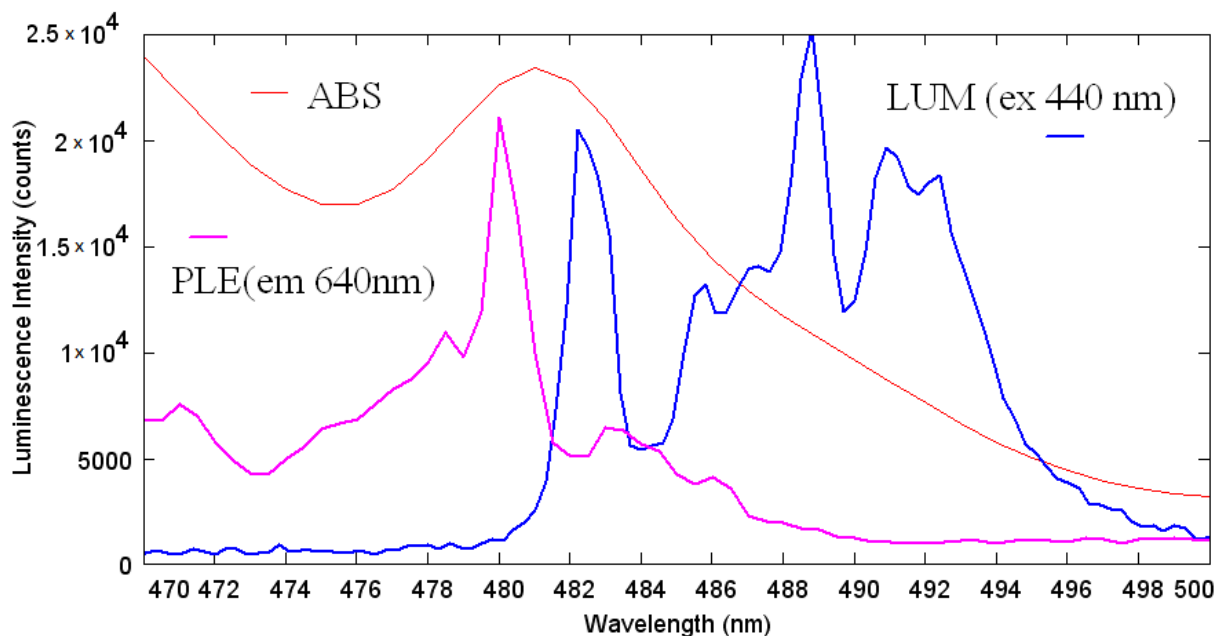
Figure 12. Excitation and emission spectra of $Pr_2(SO_4)_3$ at 77 K. The absorption spectrum at room temperature is shown for comparison.

4. Conclusions

In the present study, the structural and spectroscopic properties, and the thermal stability of $Pr_2(SO_4)_3$ have been explored for the first time. Anhydrous $Pr_2(SO_4)_3$ was synthesized by chemical precipitation in hard acids. It was found that $Pr_2(SO_4)_3$ is hydroscopic at room temperature, leading to the formation of octahydrate $Pr_2(SO_4)_3 \cdot 8H_2O$. $Pr_2(SO_4)_3$

crystallizes in the monoclinic structure with space group $C2/c$, which is typical of sulfates and molybdates of the cerium subgroup. The compound $Pr_2(SO_4)_3 \cdot 8H_2O$ is decomposed at temperatures 25–1400 °C in the argon atmosphere and does not undergo pyrohydrolysis or oxidation. The final decomposition product of $Pr_2(SO_4)_3 \cdot 8H_2O$ is the intermediate oxide Pr_6O_{11} being characteristic for the decomposition of oxygen-containing praseodymium compounds. The comparison of the emission spectra recorded at room temperature and at 77 K allowed determining the ZPL position of Pr^{3+} in $Pr_2(SO_4)_3$ at the $^3P_0 \rightarrow {}^3H_6$ transition and the accurate assignment of the rest of luminescent bands.

Supplementary Materials: The following supporting information can be downloaded at: https://www.mdpi.com/article/10.3390/molecules27133966/s1, Figure S1: The digital image of (a) $Pr_2(SO_4)_3$ and (b) $Pr_2(SO_4)_3 \cdot 8H_2O$ powder under the Sun day illumination; Figure S2: Four XRD patterns measured for the $Pr_2(SO_4)_3$ sample with 30 min intervals on keeping in the laboratory air at ambient conditions; Figure S3: Difference Rietveld plots of $Pr_2(SO_4)_3$ at different temperatures: (a) T = 30 °C; (b) T = 60 °C; (c) T = 90 °C; (d) T = 120 °C; (e) T = 150 °C; (f) T = 180 °C; (g) T = 210 °C; (h) T = 240 °C; (i) T = 270 °C; Figure S4: Brillouin zone of $Pr_2(SO_4)_3$; Figure S5: Raman spectra for $Pr_2(SO_4)_3$ recorded at 1064 and 532.1 nm excitation wavelengths; Figure S6: Comparison of the high-frequency part of Raman spectra for $Eu_2(SO_4)_3$ and $Pr_2(SO_4)_3$; Figure S7: Decomposition of the high-frequency part of $Pr_2(SO_4)_3$ Raman spectra; Figure S8: Decomposition of Raman spectra of $Pr_2(SO_4)_3$ in the range of ν_4 vibrations; Figure S9: Heat effect showing up in dependence of heating rate for processes: (a) $Pr_2(SO_4)_3 8H_2O \rightarrow Pr_2(SO_4)_3 + 8H_2O$; (b) $Pr_2(SO_4)_3 \rightarrow Pr_2O_2SO_4 + 2SO_2 + O_2$; (c) $6 Pr_2O_2SO_4 \rightarrow 2Pr_6O_{11} + 6SO_2 + O_2$ (heating rate: I-3 °C/min, II-5 °C/min, III-10 °C/min, IV-15 °C/min); Figure S10: Linearity in the manifestation of the maxima of thermal effects depending on the heating rate Table S1: Fractional atomic coordinates and isotropic displacement parameters ($Å^2$) in $Pr_2(SO_4)_3$; Table S2: Main bond lengths (Å) in $Pr_2(SO_4)_3$; Table S3: Main parameters of processing and refinement of the $Pr_2(SO_4)_3$ sample at T = 30–270 °C; Table S4: Fractional atomic coordinates (Å) and occupancies of $Pr_2(SO_4)_3 \cdot 8H_2O$; Table S5: Main bond lengths (Å) in $Pr_2(SO_4)_3 \cdot 8H_2O$.

Author Contributions: Conceptualization, Y.G.D. and V.V.A.; Data curation, Y.G.D., M.S.M., A.E.S., A.S.A., A.S.O., N.P.S., S.V.A. and I.A.R.; Formal analysis, A.S.A., A.S.O. and A.M.P.; Investigation, M.S.M., N.A.K. and E.I.S.; Supervision, O.V.A. and K.M.-B.; Writing—original draft, Y.G.D., M.S.M., A.S.A., A.S.O. and S.V.A.; Writing—review and editing, Y.G.D. and V.V.A. All authors have read and agreed to the published version of the manuscript.

Conflicts of Interest: The authors declare no conflict of interest.

References

1. Alonso, E.; Sherman, A.M.; Wallington, T.J.; Everson, M.P.; Field, F.R.; Roth, R.; Kirchain, R.E. Evaluating Rare Earth Element Availability: A Case with Revolutionary Demand from Clean Technologies. *Environ. Sci. Technol.* **2012**, *46*, 3406–3414. [CrossRef] [PubMed]
2. Baldi, L.; Peri, M.; Vandone, D. Clean energy industries and rare earth materials: Economic and financial issues. *Energy Policy* **2014**, *66*, 53–61. [CrossRef]
3. Sousa Filho, P.C.D.; de Lima, J.F.; Serra, O.A. From Lighting to Photoprotection: Fundamentals and Applications of Rare Earth Materials. *J. Braz. Chem. Soc.* **2015**, *26*, 2471–2495. [CrossRef]
4. Xia, Z.; Liu, Q. Progress in discovery and structural design of color conversion phosphors for LEDs. *Prog. Mater. Sci.* **2016**, *84*, 59–117. [CrossRef]
5. Sugimoto, S. Current status and recent topics of rare-earth permanent magnets. *J. Phys. D Appl. Phys.* **2011**, *44*, 064001. [CrossRef]
6. Xia, Z.; Zhang, Y.; Molokeev, M.S.; Atuchin, V.V. Structural and luminescence properties of yellow-emitting $NaScSi_2O_6$:Eu^{2+} phosphors: Eu2+ Ssite preference analysis and generation of red emission by codoping Mn2+ for white-light-emitting diode applications. *J. Phys. Chem. C* **2013**, *117*, 20847–20854. [CrossRef]
7. Serres, J.M.; Mateos, X.; Loiko, P.; Yumashev, K.; Kuleshov, N.; Petrov, V.; Griebner, U.; Aguiló, M.; Díaz, F. Diode-pumped microchip Tm:$KLu(WO_4)_2$ laser with more than 3 W of output power. *Opt. Lett.* **2014**, *39*, 4247–4250. [CrossRef]
8. Li, G.; Lin, C.C.; Chen, W.-T.; Molokeev, M.; Atuchin, V.V.; Chiang, C.-Y.; Zhou, W.; Wang, C.-W.; Li, W.-H.; Sheu, H.-S.; et al. Photoluminescence Tuning via Cation Substitution in Oxonitridosilicate Phosphors: DFT Calculations, Different Site Occupations, and Luminescence Mechanisms. *Chem. Mater.* **2014**, *26*, 2991–3001. [CrossRef]

9. Mutailipu, M.; Xie, Z.; Su, X.; Zhang, M.; Wang, Y.; Yang, Z.; Janjua, M.R.S.A.; Pan, S. Chemical Cosubstitution-Oriented Design of Rare-Earth Borates as Potential Ultraviolet Nonlinear Optical Materials. *J. Am. Chem. Soc.* **2017**, *139*, 18397–18405. [CrossRef]

10. Atuchin, V.V.; Subanakov, A.K.; Aleksandrovsky, A.S.; Bazarov, B.G.; Bazarova, J.G.; Dorzhieva, S.G.; Gavrilova, T.A.; Krylov, A.S.; Molokeev, M.S.; Oreshonkov, A.S.; et al. Exploration of structural, thermal, vibrational and spectroscopic properties of new noncentrosymmetric double borate Rb3NdB6O12. *Adv. Powder Technol.* **2017**, *28*, 1309–1315. [CrossRef]

11. Fischbacher, J.; Kovacs, A.; Gusenbauer, M.; Oezelt, H.; Exl, L.; Bance, S.; Schrefl, T. Micromagnetics of rare-earth efficient permanent magnets. *J. Phys. D Appl. Phys.* **2018**, *51*, 193002. [CrossRef]

12. Razumkova, I.A.; Denisenko, Y.G.; Boyko, A.N.; Ikonnikov, D.A.; Aleksandrovsky, A.S.; Azarapin, N.O.; Andreev, O.V. Synthesis and upconversion luminescence in LaF3:Yb3+, Ho3+, GdF3: Yb3+, Tm3+ and YF3:Yb3+, Er3+ obtained from sulfide precursors. *Z. Anorg. Allg. Chem.* **2019**, *645*, 1393–1401. [CrossRef]

13. Azarapin, N.O.; Aleksandrovsky, A.S.; Atuchin, V.V.; Gavrilova, T.A.; Krylov, A.S.; Molokeev, M.S.; Mukherjee, S.; Oreshonkov, A.S.; Andreev, O.V. Synthesis, structural and spectroscopic properties of orthorhombic compounds BaLnCuS3 (Ln = Pr, Sm). *J. Alloy. Compd.* **2020**, *832*, 153134. [CrossRef]

14. Lin, Z.-L.; Zeng, H.-J.; Zhang, G.; Xue, W.-Z.; Pan, Z.; Lin, H.; Loiko, P.; Liang, H.-C.; Petrov, V.; Mateos, X.; et al. Kerr-lens mode-locked Yb-SrLaAlO4 laser. *Opt. Express* **2021**, *29*, 42837–42943. [CrossRef]

15. Lim, C.-S.; Aleksandrovsky, A.; Molokeev, M.; Oreshonkov, A.; Atuchin, V. Structural and spectroscopic effects of Li+ substitution for Na+ in LixNa1-xCaGd0.5Ho0.05Yb0.45(MoO4)3 scheelite-type upconversion phosphors. *Molecules* **2021**, *26*, 7357. [CrossRef]

16. Shi, X.; Tudi, A.; Cheng, M.; Zhang, F.; Yang, Z.; Han, S.; Pan, S. Noncentrosymmetric rare-earth borate fluoride La2B5O9F3: A new ultraviolet nonlinear optical crystal with enhanced linear and nonlinear performance. *ACS Appl. Mater. Interfaces* **2022**, *14*, 18704–18712. [CrossRef]

17. Atuchin, V.; Subanakov, A.; Aleksandrovsky, A.; Bazarov, B.; Bazarova, J.; Krylov, A.; Molokeev, M.; Oreshonkov, A.; Pugachev, A. New double nonlinear-optical borate Rb3SmB6O12: Synthesis, structure and spectroscopic properties. *J. Alloy. Compd.* **2022**, *905*, 164022. [CrossRef]

18. Shannon, R.D. Revised effective ionic radii and systematic studies of interatomic distances in halides and chalcogenides. *Acta Cryst. A* **1976**, *32*, 751–767. [CrossRef]

19. Pietrelli, L.; Bellomo, B.; Fontana, D.; Montereali, M. Rare earths recovery from NiMH spent batteries. *Hydrometallurgy* **2002**, *66*, 135–139. [CrossRef]

20. Cascales, C.; Lor, B.G.; Puebla, E.G.; Iglesias, M.; Monge, M.A.; Valero, A.C.R.; Snejko, N. Catalytic Behavior of Rare-Earth Sulfates: Applications in Organic Hydrogenation and Oxidation Reactions. *Chem. Mater.* **2004**, *16*, 4144–4149. [CrossRef]

21. Perles, J.; Fortes-Revilla, C.; Gutiérrez-Puebla, E.; Iglesias, M.; Monge, M.; Ruiz-Valero, A.C.; Snejko, N. Synthesis, Structure, and Catalytic Properties of Rare-Earth Ternary Sulfates. *Chem. Mater.* **2005**, *17*, 2701–2706. [CrossRef]

22. Kul, M.; Topkaya, Y.; Karakaya, I. Rare earth double sulfates from pre-concentrated bastnasite. *Hydrometallurgy* **2008**, *93*, 129–135. [CrossRef]

23. Deng, Z.; Bai, F.; Xing, Y.; Xing, N.; Xu, L. Reaction in situ found in the synthesis of a series of lanthanide sulfate complexes and investigation on their structure, spectra and catalytic activity. *Open J. Inorg. Chem.* **2013**, *3*, 76–99. [CrossRef]

24. Huang, X.-W.; Long, Z.-Q.; Wang, L.; Feng, Z.-Y. Technology development for rare earth cleaner hydrometallurgy in China. *Rare Met.* **2015**, *34*, 215–222. [CrossRef]

25. Zhu, Z.; Pranolo, Y.; Cheng, C.Y. Separation of uranium and thorium from rare earths for rare earth production—A review. *Miner. Eng.* **2015**, *77*, 185–196. [CrossRef]

26. Jha, M.K.; Kumari, A.; Panda, R.; Kumar, J.R.; Yoo, K.; Lee, J.Y. Review on hydrometallurgical recovery of rare earth metals. *Hydrometallurgy* **2016**, *165*, 2–26. [CrossRef]

27. Diaz, L.A.; Lister, T.E.; Parkman, J.A.; Clark, G.G. Comprehensive process for the recovery of value and critical materials from electronic waste. *J. Clean. Prod.* **2016**, *125*, 236–244. [CrossRef]

28. Denisenko, Y.G.; Atuchin, V.V.; Molokeev, M.S.; Aleksandrovsky, A.S.; Krylov, A.S.; Oreshonkov, A.S.; Volkova, S.S.; Andreev, O.V. Structure, thermal stability, and spectroscopic properties of triclinic double sulfate AgEu(SO4)2 with isolated SO4 groups. *Inorg. Chem.* **2018**, *57*, 13279–13288. [CrossRef]

29. Mikhailov, M.; Yuryev, S.; Lapin, A. Prospects for applying BaSO4 powders as pigments for spacecraft thermal control coatings. *Acta Astronaut.* **2019**, *165*, 191–194. [CrossRef]

30. Zhou, Y.; Liu, X.; Lin, Z.; Li, Y.; Ding, Q.; Liu, Y.; Chen, Y.; Zhao, S.; Hong, M.; Luo, J. Pushing KTiOPO$_4$-like Nonlinear Optical Sulfates into the Deep-Ultraviolet Spectral Region. *Inorg. Chem.* **2021**, *60*, 18950–18956. [CrossRef]

31. Denisenko, Y.G.; Atuchin, V.V.; Molokeev, M.S.; Wang, N.; Jiang, X.; Aleksandrovsky, A.S.; Krylov, A.S.; Oreshonkov, A.S.; Sedykh, A.E.; Volkova, S.S.; et al. Negative thermal expansion in one-dimension of a new double sulfate AgHo(SO4)2 with isolated SO4 tetrahedra. *J. Mater. Sci. Technol.* **2021**, *76*, 111–121. [CrossRef]

32. Li, Y.; Zhou, Z.; Zhao, S.; Liang, F.; Ding, Q.; Sun, J.; Lin, Z.; Hong, M.; Luo, J. A Deep-UV Nonlinear Optical Borosulfate with Incommensurate Modulations. *Angew. Chem. Int. Ed.* **2021**, *60*, 11457–11463. [CrossRef] [PubMed]

33. Yang, H.; Xu, C.; Li, Z.; Li, M.; Liu, G. Synthesis, characterization and optical properties of three novel lanthanide sulfates. *J. Solid State Chem.* **2021**, *303*, 122481. [CrossRef]

34. Ge, Y.; Wang, Q.; Yang, F.; Huang, L.; Gao, D.; Bi, J.; Zou, G. Tin chloride sulfates A3Sn2(SO4)3−xCl1+2x (A = K, Rb, Cs; x = 0, 1) as multifunctional optical materials. *Inorg. Chem.* **2021**, *60*, 8322–8330. [CrossRef]

35. Denisenko, Y.G.; Sedykh, A.E.; Basova, S.A.; Atuchin, V.V.; Molokeev, M.S.; Aleksandrovsky, A.S.; Krylov, A.S.; Orenshonkov, A.S.; Khritokhin, N.A.; Sal'nikova, E.I.; et al. Exploration of the structural, spectroscopic and thermal properties of double sulfate monohydrate NaSm(SO4)2·H2O and its thermal decomposition product NaSm(SO4)2. *Adv. Powder Technol.* **2021**, *32*, 3943–3953. [CrossRef]

36. Song, Y.; Hao, X.; Lin, C.; Lin, D.; Luo, M.; Ye, N. Two Tellurium(IV)-Based Sulfates Exhibiting Strong Second Harmonic Generation and Moderate Birefringence as Promising Ultraviolet Nonlinear Optical Materials. *Inorg. Chem.* **2021**, *60*, 11412–11418. [CrossRef]

37. Wei, Q.; Wang, K.; He, C.; Wei, L.; Li, X.-F.; Zhang, S.; An, X.-T.; Li, J.-H.; Wang, G.-M. Linear and nonlinear optical properties of centrosymmetric Sb4O5SO4 and noncentrosymmetric Sb4O4(SO4)(OH)2 induced by lone pair stereoactivity. *Inorg. Chem.* **2021**, *60*, 11648–11654. [CrossRef]

38. Denisenko, Y.G.; Molokeev, M.S.; Oreshonkov, A.S.; Krylov, A.S.; Aleksandrovsky, A.S.; Azarapin, N.O.; Andreev, O.V.; Razumkova, I.A.; Atuchin, V.V. Crystal structure, vibrational, spectroscopic and thermochemical properties of double sulfate crystalline hydrate [CsEu(H2O)3(SO4)2]·H2O and its thermal dehydration product CsEu(SO4)2. *Crystals* **2021**, *11*, 1027. [CrossRef]

39. Han, Y.; Zhao, X.; Xu, F.; Li, B.; Ye, N.; Luo, M. HgSO4: An excellent mid-infrared sulfate nonlinear optical crystal with wide band gap and strong second harmonic generation response. *J. Alloy. Compd.* **2022**, *902*, 163727. [CrossRef]

40. Shen, Y.; Tang, W.; Lin, X. Advances in second-order nonlinear optical sulfates. *Coord. Chem. Rev.* **2022**, *459*, 214443. [CrossRef]

41. Wu, C.; Jiang, X.; Hu, Y.; Jiang, C.; Wu, T.; Lin, Z.; Huang, Z.; Humphrey, M.G.; Zhang, C. A Lanthanum Ammonium Sulfate Double Salt with a Strong SHG Response and Wide Deep-UV Transparency. *Angew. Chem. Int. Ed.* **2021**, *61*, e202115855. [CrossRef]

42. Sirotinkin, S.P.; Efremov, V.A.; Kovba, L.M.; Pokrovskij, A.N. Crystal structure of anhydrous neodymium sulfate Nd2(SO4)3. *Kristallografiya* **1977**, *22*, 1272–1273.

43. Denisenko, Y.G.; Aleksandrovsky, A.S.; Atuchin, V.V.; Krylov, A.S.; Molokeev, M.S.; Oreshonkov, A.S.; Shestakov, N.P.; Andreev, O.V. Exploration of structural, thermal and spectroscopic properties of self-activated sulfate Eu2(SO4)3 with isolated SO4 groups. *J. Ind. Eng. Chem.* **2018**, *68*, 109–116. [CrossRef]

44. Wickleder, M.S. Wasserfreie sulfate der selten-erd-elemente: Synthese und kristallstruktur von Y2(SO4)3 und Sc2(SO4)3. *Z. Anorg. Allg. Chem.* **2000**, *626*, 1468–1472. [CrossRef]

45. Wickleder, M.S. Sulfate und hydrogensulfate des erbiums: Er(HSO4)3-I, Er(HSO4)3-II, Er (SO4)(HSO4) und Er2(SO4)3. *Z. Anorg. Allg. Chem.* **1998**, *624*, 1347–1354. [CrossRef]

46. Wickleder, M.S. Inorganic Lanthanide Compounds with Complex Anions. *Chem. Rev.* **2002**, *102*, 2011–2088. [CrossRef]

47. Mills, S.J.; Petříček, V.; Kampf, A.R.; Herbst-Imer, R.; Raudsepp, M. The crystal structure of Yb2(SO4)3·3H2O and its decomposition product, β-Yb2(SO4)3. *J. Solid State Chem.* **2011**, *184*, 2322–2328. [CrossRef]

48. Machida, M.; Kawano, T.; Eto, M.; Zhang, D.; Ikeue, K. Ln Dependence of the Large-Capacity Oxygen Storage/Release Property of Ln Oxysulfate/Oxysulfide Systems. *Chem. Mater.* **2007**, *19*, 954–960. [CrossRef]

49. Liang, J.; Ma, R.; Geng, F.; Ebina, Y.; Sasaki, T. Ln2(OH)4SO4·nH2O (Ln = Pr to Tb; n ∼ 2): A new family of layered rare-earth hydroxides rigidly pillared by sulfate ions. *Chem. Mater.* **2010**, *22*, 6001–6007. [CrossRef]

50. Atuchin, V.; Gavrilova, T.; Grivel, J.-C.; Kesler, V.; Troitskaia, I. Electronic structure of layered ferroelectric high-k titanate Pr2Ti2O7. *J. Solid State Chem.* **2012**, *195*, 125–131. [CrossRef]

51. Dannenbauer, N.; Matthes, P.R.; Müller-Buschbaum, K. Luminescent coordination polymers for the VIS and NIR range constituting from LnCl3 and 1,2-bis(4-pyridyl)-ethane. *Dalton Trans.* **2016**, *45*, 6529–6540. [CrossRef] [PubMed]

52. Dannenbauer, N.; Matthes, P.R.; Scheller, T.P.; Nitsch, J.; Zottnick, S.H.; Gernert, M.S.; Steffen, A.; Lambert, C.; Müller-Buschbaum, K. Near-infrared luminescence and inner filter effects of lanthanide coordination polymers with 1,2-Di(4-pyridyl)ethylene. *Inorg. Chem.* **2016**, *55*, 7396–7406. [CrossRef] [PubMed]

53. Ridenour, J.A.; Carter, K.P.; Cahill, C.L. RE-p-halobenzoic acid–terpyridine complexes, part III: Structural and supramolecular trends in a series of p-iodobenzoic acid rare-earth hybrid materials. *CrystEngComm* **2017**, *19*, 1190–1203. [CrossRef]

54. Sedykh, A.E.; Kurth, D.G.; Müller-Buschbaum, K. Two series of lanthanide coordination polymers and complexes with 4'-phenylterpyridine and their luminescence properties. *Eur. J. Inorg. Chem.* **2019**, *2019*, 4564–4571. [CrossRef]

55. Vaiano, V.; Matarangolo, M.; Sacco, O.; Sannino, D. Photocatalytic treatment of aqueous solutions at high dye concentration using praseodymium-doped ZnO catalysts. *Appl. Catal. B Environ.* **2017**, *209*, 621–630. [CrossRef]

56. Jin, Q.; Shen, Y.; Zhu, S.; Liu, Q.; Li, X.; Yan, W. Effect of praseodymium additive on CeO2(ZrO2)/TiO2 for selective catalytic reduction of NO by NH3. *J. Rare Earths* **2016**, *34*, 1111–1120. [CrossRef]

57. Najjar, H.; Batis, H.; Lamonier, J.-F.; Mentré, O.; Giraudon, J.-M. Effect of praseodymium and europium doping in La1−xLnxMnO3+δ (Ln: Pr or Eu, 0 ≤ x ≤ 1) perosvkite catalysts for total methane oxidation. *Appl. Catal. A* **2014**, *469*, 98–107. [CrossRef]

58. Jin, Q.; Shen, Y.; Zhu, S. Praseodymium oxide modified CeO2/Al2O3 catalyst for selective catalytic reduction of NO by NH3. *Chin. J. Chem.* **2016**, *34*, 1283–1290. [CrossRef]

59. Guillén-Hurtado, N.; García-García, A.; Bueno-López, A. Active oxygen by Ce–Pr mixed oxide nanoparticles outperform diesel soot combustion Pt catalysts. *Appl. Catal. B* **2015**, *174*, 60–66. [CrossRef]

60. Sato, K.; Imamura, K.; Kawano, Y.; Miyahara, S.-I.; Yamamoto, T.; Matsumura, S.; Nagaoka, K. A low-crystalline ruthenium nano-layer supported on praseodymium oxide as an active catalyst for ammonia synthesis. *Chem. Sci.* **2017**, *8*, 674–679. [CrossRef]

61. Bartl, M.H.; Gatterer, K.; Cavalli, E.; Speghini, A.; Bettinelli, M. Growth, optical spectroscopy and crystal field investigation of YAl3(BO3)4 single crystals doped with tripositive praseodymium. *Spectrochim. Acta Part A Mol. Biomol. Spectrosc.* **2001**, *57*, 1981–1990. [CrossRef]

62. Guzik, M.; Aitasalo, T.; Szuszkiewicz, W.; Hölsä, J.; Keller, B.; Legendziewicz, J. Optical spectroscopy of yttrium double phosphates doped by cerium and praseodymium ions. *J. Alloy. Compd.* **2004**, *380*, 368–375. [CrossRef]

63. Pisarski, W.A. Spectroscopic analysis of praseodymium and erbium ions in heavy metal fluoride and oxide glasses. *J. Mol. Struct.* **2005**, *744–747*, 473–479. [CrossRef]

64. Utikal, T.; Eichhammer, E.; Petersen, L.; Renn, A.; Götzinger, S.; Sandoghdar, V. Spectroscopic detection and state preparation of a single praseodymium ion in a crystal. *Nat. Commun.* **2014**, *5*, 3627. [CrossRef]

65. Feng, X.; Feng, W.; Wang, K. Experimental and theoretical spectroscopic study of praseodymium(III) doped strontium aluminate phosphors. *J. Alloy. Compd.* **2015**, *628*, 343–346. [CrossRef]

66. Wang, X.; Li, J.-G.; Molokeev, M.S.; Zhu, Q.; Li, X.; Sun, X. Layered hydroxyl sulfate: Controlled crystallization, structure analysis, and green derivation of multi-color luminescent (La,RE) 2 O 2 SO 4 and (La,RE) 2 O 2 S phosphors (RE = Pr, Sm, Eu, Tb, and Dy). *Chem. Eng. J.* **2016**, *302*, 577–586. [CrossRef]

67. Chen, H.-L.; Wei, L.-K.; Chang, Y.-S. Characterizations of Pr3+ Ion-Doped LaVO4 Phosphor Prepared Using a Sol–Gel Method. *J. Electron. Mater.* **2018**, *47*, 6649–6654. [CrossRef]

68. Tian, X.; Li, J.; Sheng, H.; Li, T.; Guo, L.; Ji, C.; Huang, Z.; Wen, J.; Liu, X.; Li, C.; et al. Luminescence and optical thermometry based on silico-carnotite Ca3Y2Si3O12: Pr3+ phosphor. *Ceram. Int.* **2021**, *48*, 3860–3868. [CrossRef]

69. Bruker. *Bruker AXS TOPAS V4*; Bruker: Karlsruhe, Germany, 2008.

70. Clark, S.J.; Segall, M.D.; Pickard, C.J.; Hasnip, P.J.; Probert, M.I.J.; Refson, K.; Payne, M.C. First Principles Methods Using CASTEP. *Z. Kristallogr. Cryst. Mater.* **2005**, *220*, 567–570. [CrossRef]

71. Perdew, J.P.; Zunger, A. Self-interaction correction to density-functional approximations for many-electron systems. *Phys. Rev. B* **1981**, *23*, 5048–5079. [CrossRef]

72. Ceperley, D.M.; Alder, B.J. Ground State of the Electron Gas by a Stochastic Method. *Phys. Rev. Lett.* **1980**, *45*, 566–569. [CrossRef]

73. *NETZSCH Proteus 6, Thermic Analyses e User's and Software Manuals*; NETZSCH: Selb, Germany, 2012.

74. Blaine, R.L.; Kissinger, H.E. Homer Kissinger and the Kissinger equation. *Thermochim. Acta* **2012**, *540*, 1–6. [CrossRef]

75. Bukovec, N.; Bukovec, P.; Šiftar, J. Kinetics of the thermal decomposition of Pr2(SO4)3 to Pr2O2SO4. *Thermochim. Acta* **1980**, *35*, 85–91. [CrossRef]

76. Lyadov, A.S.; Kurilkin, V.V. Reduction specifics of rare-earth orthovanadates (REE = La, Nd, Sm, Dy, Ho, Er, Tm, Yb, and Lu). *Russ. J. Inorg. Chem.* **2016**, *61*, 86–92. [CrossRef]

77. Llópiz, J.; Romero, M.; Jerez, A.; Laureiro, Y. Generalization of the kissinger equation for several kinetic models. *Thermochim. Acta* **1995**, *256*, 205–211. [CrossRef]

78. Sirotinkin, S.P. Physicochemical Study of Double Sulfates of Lithium and Rare Earth Elements. D.Sc. Thesis, Moscow State University, Moscow, Russia, 1978.

79. Favre-Nicolin, V.; Černý, R. FOX: Modular Approach to Crystal Structure Determination from Powder Diffraction. *Mater. Sci. Forum* **2004**, *443–444*, 35–38. [CrossRef]

80. Favre-Nicolin, V.; Černý, R. FOX, free objects for crystallography: A modular approach to ab initio structure determination from powder diffraction. *J. Appl. Crystallogr.* **2002**, *35*, 734–743. [CrossRef]

81. Spek, A.L. Single-crystal structure validation with the program *PLATON*. *J. Appl. Crystallogr.* **2003**, *36*, 7–13. [CrossRef]

82. Brown, I.D.; Altermatt, D. Bond-valence parameters obtained from a systematic analysis of the Inorganic Crystal Structure Database. *Acta Crystallogr. Sect. B Struct. Sci. Cryst. Eng. Mater.* **1985**, *B41*, 244–247. [CrossRef]

83. Blatov, V.A.; Shevchenko, A.P.; Proserpio, D.M. Applied Topological Analysis of Crystal Structures with the Program Package ToposPro. *Cryst. Growth Des.* **2014**, *14*, 3576–3586. [CrossRef]

84. Kroumova, E.; Aroyo, M.I.; Mato, J.M.P.; Kirov, A.; Capillas, C.; Ivantchev, S.; Wondratschek, H. Bilbao Crystallographic Server: Useful Databases and Tools for Phase-Transition Studies. *Phase Transit.* **2003**, *76*, 155–170. [CrossRef]

85. Nakamoto, N. *Infrared and Raman Spectra of Inorganic and Coordination Compounds*, 6th ed.; Wiley: New York, NY, USA, 2009.

86. Blatov, V.A.; Peskov, M.V. A comparative crystallochemical analysis of binary compounds and simple anhydrous salts containing pyramidal anions LO3 (L = S, Se, Te, Cl, Br, I). *Acta Crystallogr. Sect. B Struct. Sci.* **2006**, *62*, 457–466. [CrossRef] [PubMed]

87. Poston, J.A., Jr.; Siriwardane, R.V.; Fisher, E.P.; Miltz, A.L. Thermal decomposition of the rare earth sulfates of cerium (III), cerium (IV), lanthanum (III) and samarium (III). *Appl. Surf. Sci.* **2003**, *214*, 83–102. [CrossRef]

88. Andreev, O.V.; Denisenko, Y.G.; Osseni, S.A.; Bamburov, V.G.; Sal'nikova, E.I.; Khritokhin, N.A.; Andreev, P.O.; Polkovnikov, A.A. *Sulfates and Oxysulfides of Rare-Earth Elements*; UTMN Publishing: Tyumen, Russia, 2017.

89. Stubblefield, C.T.; Eick, H.; Eyring, L. Praseodymium Oxides. III. The Heats of Formation of Several Oxides1. *J. Am. Chem. Soc.* **1956**, *78*, 3018–3020. [CrossRef]

90. Eckman, J.R.; Rossini, F.D. The heat of formation of sulphur dioxide. *Bur. Stand. J. Res.* **1929**, *3*, 597–618. [CrossRef]

91. Rossini, F.D. The heat of formation of water. *Proc. Natl. Acad. Sci. USA* **1930**, *16*, 694–699. [CrossRef]

92. Denisenko, Y.; Khritokhin, N.; Andreev, O.; Basova, S.; Sal'Nikova, E.; Polkovnikov, A. Thermal decomposition of europium sulfates Eu2(SO4)3·8H2O and EuSO4. *J. Solid State Chem.* **2017**, *255*, 219–224. [CrossRef]
93. Irtyugo, L.A.; Denisova, L.T.; Molokeev, M.S.; Denisov, V.M.; Aleksandrovsky, A.S.; Beletskii, V.V.; Sivkova, E.Y. Synthesis, Crystal Structure, and the Optical and Thermodynamic Properties of PrAlGe2O7. *Russ. J. Phys. Chem. A* **2021**, *95*, 1546–1550. [CrossRef]
94. Denisova, L.T.; Molokeev, M.S.; Kargin, Y.F.; Gerasimov, V.P.; Krylov, A.S.; Aleksandrovskii, A.S.; Chumilina, L.G.; Denisov, V.M.; Vasil'ev, G.V. Synthesis, crystal structure, and physicochemical properties of Bi4–xPrxTi3O12 (x = 0.4, 0.8, 1.2, 1.6) solid solutions. *Inorg. Mater.* **2021**, *57*, 919–928. [CrossRef]
95. Srivastava, A.M. Aspects of Pr3+ luminescence in solids. *J. Lumin.* **2016**, *169*, 445–449. [CrossRef]